A PRELIMINARY ANALYSIS OF THE ABILITY OF A POTENTIAL ORTHOTIC DEVICE TO REDUCE AND MITIGATE SHOE SLIP

by

K. Beauwen Freckleton

A thesis submitted to the faculty of
The University of Utah
in partial fulfillment of the requirements for the degree of

Master of Science

Department of Mechanical Engineering

The University of Utah

August 2017

The University of Utah Graduate School

STATEMENT OF THESIS APPROVAL

The thesis of **K. Beauwen Freckleton**

has been approved by the following supervisory committee members:

Mark A. Minor	, Chair	**05/10/17** Date Approved
Andrew Merryweather	, Member	**05/10/17** Date Approved
Sanford G. Meek	, Member	**05/10/17** Date Approved

and by **Tim Ameel**, Chair/Dean of

the Department/College/School of **Mechanical Engineering**

and by David B. Kieda, Dean of The Graduate School.

ABSTRACT

This research explores the potential for an “intelligent” orthotic shoe sole to negate, or minimize, longitudinal slip by momentarily increasing friction force. The conceptual device takes the form of a rubberized shoe sole containing pockets of air that can be released via valves controlled by a microprocessor. During a slip event, the valves would be opened and the bladders would be collapsed by the weight of the user, which modulates contact and friction forces. The goal is to increase friction forces in this process, by creating an impact force between the user and ground surface, with the potential to achieve stiction and stop slip.

The research first explores how design of the shoe sole can best compensate for longitudinal slip. Lumped parameter models of the system are developed to model bladder behavior and airflow through the system, which are then applied to optimize a prototype design. A friction model specific for two sliding surfaces is developed using basic coulombic friction equations. Simulations and experiments indicated flow rate was a limiting factor using existing valves, but experiments without valves confirmed that impact forces and friction forces can be increased by the system.

The impulse created during impact creates a large spike in normal force, which translates into a spike in coulombic friction force that can be mathematically shown to reduce slipping velocity. The spike also causes an increase in Coefficient of Friction (COF) with the shoe and ground surface that, with surface specific testing, can be used to shift the sliding foot from a potentially dangerous kinetic COF range to a more stable static COF. Results of kinematic modeling are presented as well as empirical testing and future work.

TABLE OF CONTENTS

1. INTRODUCTION

The ability to walk is the most basic form of human mobility and yet represents one of the most dangerous scenarios for human disability. This danger stems from the potential to fall, due to shoe slip, which affects both the elderly and the laborers in a workplace. Liberty Mutual Institute Research Institute for Safety reported an almost 37% increase in reported same level falls in the first decade of the 20th century. These falls represent $7.7 billion dollars per year in terms of cost due to disabling injury, deeming it the second most disabling type of injury [1]. While many studies have investigated the cognitive response of humans to slip, the approach in this thesis delves into the possibility of an "intelligent" shoe or orthotic device capable of reducing or possibly nullifying human slip.

Slip occurs when the required coefficient of friction (COF) to maintain traction with the surface is greater than the available COF of the surface. The approach in this thesis consists of the development of a slip scenario simulation via MATLAB Simulink software that utilizes a mathematical approach to model a proposed orthotic device that could be utilized to mitigate slip. The construction and subsequent empirical testing of the device is then detailed in order to validate the mathematical model as well as determine if the design can achieve slip-mitigating properties. A concept of the orthotic device, discussed throughout the thesis, is shown in Figure 1.1. The device is composed of a series of air bladders, each incorporating a microcontroller and four (4) solenoid valves to release air out of the bladder system. In future work, as described in Chapter 5, the bladders will also possibly contain a series of accelerometers, gyroscopes, strain

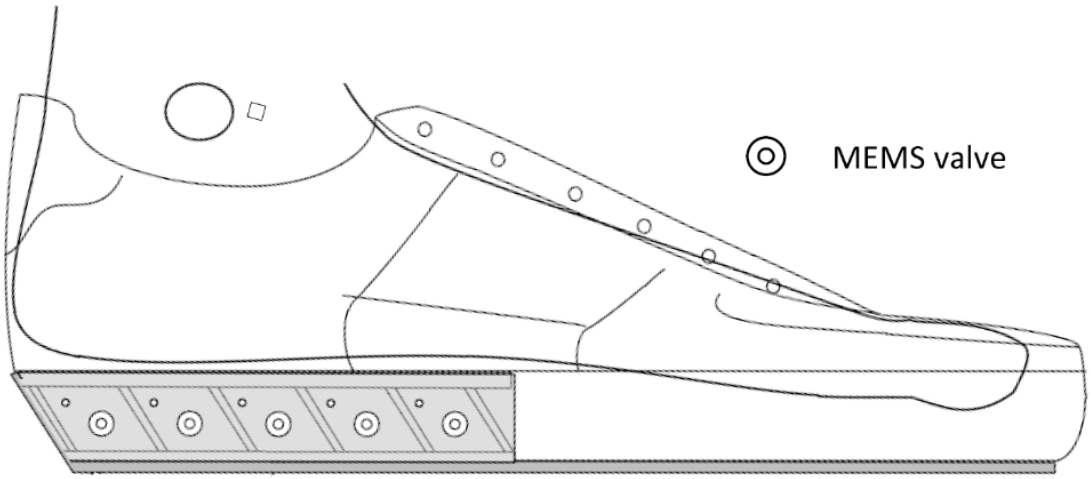

Figure 1.1: Concept of intelligent orthotic device showing bladder system with valves. The bladders of air are separated by angled lines in the heel of the shoe sole. Icons representing the possible location of air release valves are provided.

gauges, and other sensors. While the construction of the electrical components and bladder molding process is detailed in other works [2] [3], this thesis focuses on the design and kinematics of the bladder system in order to create slip-preventing/mitigating forces.

The mathematical model analyzes the directional compliancy in the bladder walls, the air pressure in the bladders, the air flow out of the bladders, the contact of the top and bottom of the bladders, and the corresponding friction force generated by the normal or contact force. The friction force is determined using a coulombic friction mode that incorporates stiction applied continuously to four independent surfaces.

The proposed hypothesis explores the possibility of generating a brief spike in available friction force between the ground and shoe that is created after the bladders are popped and the user experiences a somewhat free fall collision with the shoe sole and ground. The collision creates an impulse spike in normal force that translates into a spike in available friction force

and possible spike in COF. Equation (1.1) is the basis of Coulombic friction where the friction forces are proportional to the normal force, F_N, of the surfaces of impact and μ, the proportionality constant, is most often determined empirically. Note that the equation uses an F_{fmax} term, which denotes the surfaces are on the verge of slip,

$$F_{fmax} = \mu F_N sgn(v_x) \tag{1.1}$$

The typical equation used to model impact or impulse commonly takes the form of equation (1.2)

$$\int_{t_1}^{t_2} F dt = m\Delta v \tag{1.2}$$

where F is the applied force, t is the duration of time the force is applied, and $m\Delta v$ is the change in momentum where m is the mass of the object in collision and v is the velocity of the mass. Before bladder actuation, or the opening of the valves and release of air, the normal force N acting on the shoe is simply the weight of the user, as the mass of the shoe is negligible. When the user's foot strikes the ground, a normal force greater than that due to gravity is created by the impact that is termed N_i. Substituting N_i for F_N in equation (1.1) yields

$$F_f = \mu N_i sgn(v_x) \tag{1.3}$$

and substituting F_f from equation (1.3) into F as well as M_1, which is termed the weight of the user, into m from equation (1.2) yields

$$\int_{t_1}^{t_2} \mu N_i sgn(v_x) dt = M_1 \Delta v \tag{1.4}$$

where μ depends on whether the system is sliding or sticking when the impact occurs. Rearranging equation (1.4) yields

$$\frac{1}{M_1} \int_{t_1}^{t_2} F_f dt = \Delta v \tag{1.5}$$

which is the primary equation used to determine if slip speed/momentum reduction or stopping is possible by manipulation of the impulse.

2. RELATED WORK

The study of slipping phenomena dynamics in relation to human gait has been repeatedly analyzed using subject testing. Several conclusions of key slip indicators, such as critical slip distance and critical slip velocity, have been explored in order to predict the slipping phenomena. Strandberg and Lanshammar found that during subject testing, a “dangerous” slip indicator, or a slip that would usually result in a fall, would occur if the foot sliding motion exceeded 0.5 m/s or a slip distance in excess of 10 cm [4]. Cham and Redfern [5] conducted a similar subject test using inclined surfaces and different contaminants while recording foot motion. They determined that many variables, such as heel acceleration, are important to slip phenomena, but also concluded that the dangerous slip criteria from Strandberg and Lanshammar were consistent with their own results. It is interesting to note that Strandberg and Lanshammar found that small slip occurrences, both in a forward and reverse direction of motion, are typical aspects of “normal” gait. However, under less than ideal surface conditions, these slip occurrences can grow to unstable levels and enter the aforementioned “dangerous” slip zone that typically results in injury-causing falling. They also discovered that many slip instances, where slip velocity and slip distance do not exceed these critical points, result in slip-recovery instances where the user loses stability momentarily but is able to recover from the slip and avoid falling. Perkins [6] conducted a similar test that focused on the relationship of horizontal and normal forces during slip activity and concluded that slip severity, or loss of balance, was dependent on slip distance exceeding 10 – 15 cm in length. Their results agreed

with those found by Strandberg and Lanshammar as well as Cham and Redfern. While kinematics of slip are not largely studied in this thesis, it is proposed that, in future work, these kinds of studies can be used in conjunction with the proposed orthotic device to reduce the danger of or prevent slip phenomena. Note that physiological factors such as age and gender were not used in the three studies mentioned above. Future studies that analyze the effects of age, health, work environment, etc. would contribute to determining a more specific slip criteria based on individual user circumstance. However, the results can still provide a reasonable baseline for slip prediction throughout this thesis. Although the concepts in this thesis of a slip mitigating orthotic device can potentially be applied to a variety of user circumstances, the targeted groups are most likely an elderly population who are more prone to falls and companies who carry worker's compensation risks for employees.

"Intelligent" shoe design has been applied in many areas relating to human gait. Wahab designed a low-cost intelligent shoe that analyzes factors relating to gait such as kinematics, pressure, and orientation for use in medical and athletic improvement [7]. Nguyen used an intelligent shoe as an innovative approach to terrain mapping with possible application for people with disabilities such as blindness or for high-risk scenarios such as those experienced by firefighters [8]. Intelligent shoe design in relation to slip has been studied by Tao who developed a shoe that learns, recognizes, and detects human fall directions [9]. In relation to preventing falls from occurring, Onodera developed an intelligent shoe that uses a parallel linkage system to enlarge the surface area of the shoe sole and thereby increase stability of the person [10]. The intelligent shoe design in this thesis discusses the potential of an orthotic device that, when actuated, could prevent or mitigate slip during human gait activity by manipulating the friction forces between the shoe and ground.

The study of friction in relation to human gait surfaces is one of the primary concerns when designing buildings for safety, especially in an industrial type workplace. Many studies within this area seek to find the required coefficient of friction (RCOF) between the shoe and floor surface needed to maintain stiction [11] [12] [13]. In terms of simulating friction, however, challenges such as nonlinearities and discontinuities when velocity is zero make coulombic friction modeling more difficult and it is application specific. Kikuuwe created two models that analyzed continuous and discontinuous (at v=0) situations in order to compare the pros and cons of each [14]. Simulating stiction also poses a challenge that is often application specific. Many models utilize a Pseudo-Coulombic friction model where, instead of modeling stiction, the relative velocity of the contacting surfaces is deemed negligibly small [15]. When stiction is necessary for the simulation, a more complex model that switches between stiction to no-stiction is used [16] [17]. These models often incorporate an arbitrary threshold value that generally translates to a low relative velocity between the surfaces deemed as $v \approx 0$ [18]. The model used in this thesis incorporates this stiction to non-stiction type modeling as stopping slip is a primary objective within this thesis.

Because ground contact forces are a primary focus of this study in relation to the effectiveness of the orthotic device in minimizing dangerous slip phenomena, it is necessary to include a brief literature review of contact modeling mechanics. A variety of contact algorithms are used when representing biped-type objects colliding with a ground surface. Wensing [19] and de Lasa [20] employed an algorithm that modeled ground contact forces by commanding the feet of biped robots to remain in contact with the ground and not to accelerate. A more complex model was created for quadruped robots by Park [21] that utilizes Bezier polynomial equations. However, some of the more popular contact models are modifications of the Hertz

Law [22], which dates back to the late 1800s, shown in equation (2.1). *K* and *n* are contact stiffness parameters and *n* is typically equal to 3/2 [23] [24].

$$F_N = K\delta^n \tag{2.1}$$

The Hertz law focuses purely on elastic forces and is therefore applicable to a small range of situations. Introduction of the Kelvin-Voight model, shown as equation (2.2), accounted for viscous or dissipative forces where *D* is a damping parameter [25].

$$F_N = K\delta^n + D\dot{\delta} \tag{2.2}$$

Several adaptations of the Kelvin-Voight model have repeatedly surfaced including the model used by Aguirre, shown as equation (2.3) for a biped robot [26] where c_r is the coefficient of restitution.

$$F_N = -c_r|\delta|^n\delta - \dot{K}|\delta|^n \tag{2.3}$$

Other adaptations, such as that done by Flores in equation (2.4), have sought to adapt the Kelvin-Voight model to work for softer or compliant materials that dissipate larger amounts of energy [23].

$$F_N = K\delta^n\left[1 + \frac{8(1-c_r)}{5c_r}\frac{\dot{\delta}}{\delta^{(\dot{-})}}\right] \tag{2.4}$$

Others attempt to make a more generalized model for all material types such as that proposed by Gonthier in equation (2.5) [27].

$$F_N = K\delta^n\left[1 + \frac{1-{c_r}^2}{c_r}\frac{\dot{\delta}}{\delta^{(\dot{-})}}\right] \tag{2.5}$$

Equations (2.4) and (2.5), known as the Flores and Gonthier models throughout this thesis, were found to predict similar results when simulated by Machado [24]. These two models are used in this thesis and are discussed further in context.

3. DEVELOPMENT OF BLADDER MODEL

This chapter outlines the iterative process of creating a MATLAB Simulink model to describe the dynamics of the proposed orthotic device and analyze the capability of using the device to mitigate slip. The culmination of the models discussed in the next section leads to the model shown in Figure 3.1. The model is presented here for reference throughout the chapter. The various components of the figure will be discussed in their respective sections below.

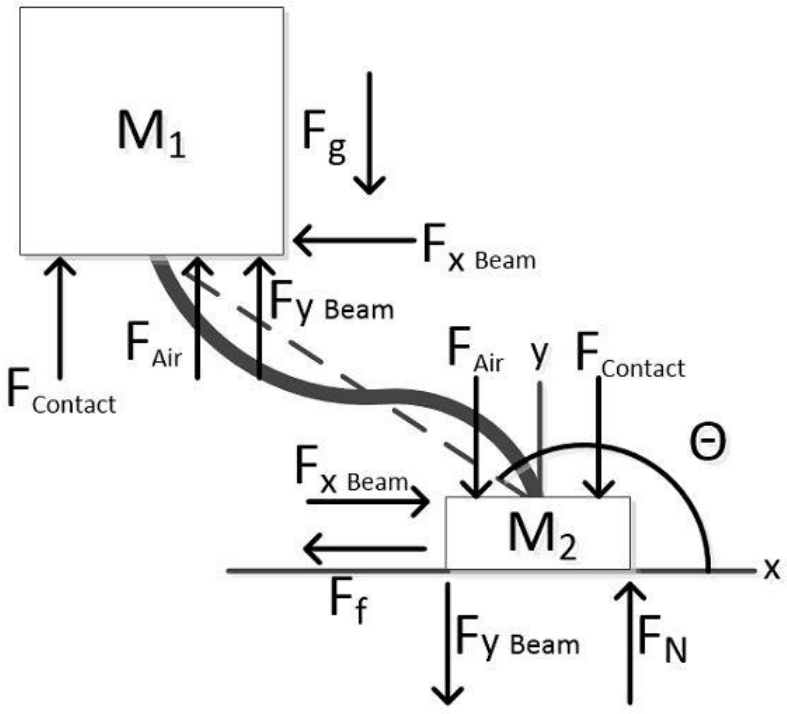

Figure 3.1: Final simulation schematic, or the culmination of all the proceeding simulation models. The schematic is shown here for reference throughout the chapter. In the figure, F_g is the force of the masses due to gravity, F_{air} is the force of air due to bladder pressure, $F_{()Beam}$ are the forces due to the bladder wall structure, F_N is the normal force, and $F_{Contact}$ are forces due to the two masses contacting. All other components will be discussed in context below. The figure will be used in simulation at the ending section of this chapter.

Linear Beam Structure Model

The modeling of the proposed orthotic device is done iteratively and focused primarily on understanding kinematics of the system. The goal of this procedure is to understand the behavior of the directionally compliant bladder structure, and the impact forces generated during actuation under slipping scenarios.

Figure 3.2 depicts the basic bladder wall structure schematic of the proposed orthotic device before and after gait activity. Post-buckled beam theory is assumed to describe the behavior of the inner bladder walls and they are often referred to as beams throughout this thesis. The outer bladder walls, due to the complexity, are difficult to model and are accounted for empirically in Chapter 4. M_1 represents the mass of the person or more simply the foot acting as a mass exerting a downward compressive force on the slanted beam structure of the bladders. M_1 is assumed to be in free fall for a simplistic iterative approach to understanding the kinematics of the bladder structure, F_x and F_y represent the reaction forces from the beam due to the falling mass, and θ is the angle between the beam walls and the horizontal.

A single beam is used for kinematic demonstration purposes and analysis. It should be noted that in Figure 3.2, the force exerted by the air pressure build up in the bladders of the proposed device to hold M_1 aloft is not accounted for initially but will be discussed later in this chapter. Contact between M_1 and the ground is also simulated using the contact equations discussed later in this chapter.

The slanted bladder walls exert both horizontal and vertical forces on M_1 upon collapsing while the other end of the beam is fixed. This fixation of one beam end is, again, part of the simplistic iterative approach.

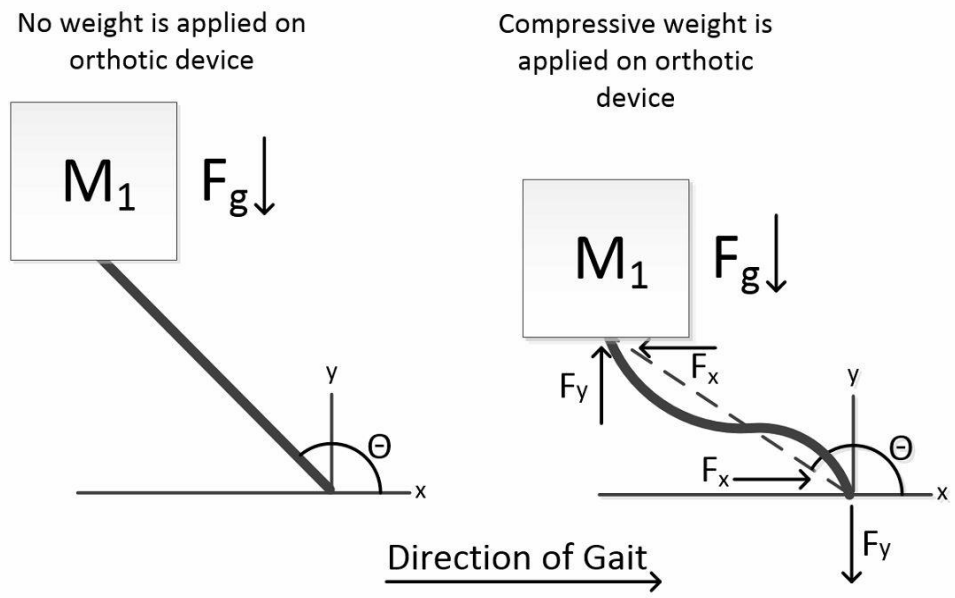

Figure 3.2: Basic schematic of collapsing foot on slanted beam.

We assume simple beam theory when modeling the wall. However, this theory is limited by the large deflections compared to wall lengths. Empirical testing in Chapter 4 shows a more descriptive validation of this model. The stiffness on any horizontal beam can be modeled [28] by using equation (3.1)

$$K = \begin{bmatrix} K_{xx} & K_{xy} \\ K_{yx} & K_{yy} \end{bmatrix} \tag{3.1}$$

where,

$$K_{xx} = \frac{EI}{L^3}\begin{bmatrix} \frac{\pi^2}{2} & 0 & 0 \\ 0 & 12 & 6L \\ 0 & 6L & 4L^2 \end{bmatrix}$$

$$K_{xy} = \frac{EI}{L^3}\begin{bmatrix} -\frac{\pi^2}{2} & 0 & 0 \\ 0 & -12 & 6L \\ 0 & -6L & 4L^2 \end{bmatrix}$$

$$K_{yx} = K_{xy}^T$$

$$K_{yy} = \frac{EI}{L^3}\begin{bmatrix} \frac{\pi^2}{2} & 0 & 0 \\ 0 & 12 & -6L \\ 0 & -6L & 4L^2 \end{bmatrix}$$

and the axial stiffness for a beam in post-buckled position is described [29] by

$$\frac{EI}{2} * \frac{\pi^2}{L^3}$$

where *E* is the Young's modulus constant for the material, *L* is the length of the beam, and *I* is the moment of inertia, which is,

$$I = \frac{bh^3}{12} \tag{3.2}$$

The length of the wall parallel to the ground is represented by *b* and *h* is the wall thickness. The material that will be used for later prototyping is *Smooth-On, Mold Max 40* [30]. For simplicity in this early design phase, the beam is assumed to have a linear spring constant and modulus of elasticity. The material was tested to determined mechanical properties such as Young's Modulus, *E*, as being roughly $3 * 10^6$MPa [2]. We assume *b* to be about 90 mm or 3.54 in., *L* to be 24 mm or 1 in., and *h* to be 5 mm or 0.2 in. The values for *b* and *L* were chosen arbitrarily based on a U.S. size 11.5 shoe sole while *h* was determined analytically through the simulations discussed below as one possible option for shoe sole design.

It was assumed that the moments on the ends of the beams were negligible due to the compliant nature of the material, and thus θ was removed from the model such that equation (3.1) can be reduced to equation (3.3)

$$K' = \begin{bmatrix} K'_{xx} & K'_{xy} \\ K'_{yx} & K'_{yy} \end{bmatrix} \tag{3.3}$$

where,

$$K'_{xx} = \frac{EI}{L^3}\begin{bmatrix} \frac{\pi^2}{2} & 0 \\ 0 & 12 \end{bmatrix}$$

$$K'_{xy} = \frac{EI}{L^3}\begin{bmatrix} -\frac{\pi^2}{2} & 0 \\ 0 & -12 \end{bmatrix}$$

$$K'_{yx} = K'_{xy}$$

$$K'_{yy} = K'_{xx}$$

The proposed dynamic model of Figure 3.2 was simulated using MATLAB Simulink software. The goals of this simulation were to characterize the motion of the compliant beam under gait forces. The equations of motion used in the simulation are derived as follows, starting with equation (3.4):

$$M_1\ddot{x} + B\dot{x} + K'x = F(x) \tag{3.4}$$

M_1 is, again, the mass of the human (or force pushing down on the beam), B is the damping force coefficient within the spring, and K' is mentioned earlier in equation (3.3). The mass is then divided throughout all terms to form equation (3.5).

$$\ddot{x} + \frac{B}{M}\dot{x} + \frac{K'}{M}x = \hat{f}(x) \tag{3.5}$$

To find B, equation (3.5) is rearranged as equation (3.6),

$$\ddot{x} + 2\xi\omega_n\dot{x} + \omega_n^2 x = \hat{f}(x) \tag{3.6}$$

where ω_n is the natural frequency and

$$B = 2\xi\sqrt{K'M} \tag{3.7}$$

ξ is chosen arbitrarily as 0.9 as the impact of the person on the orthotic device sole is expected to be nearly critically damped based upon prior observations. The stiffness matrix K' is derived for a horizontal beam; therefore, a standard rotation matrix R, given in equation (3.8),

$$R = \begin{bmatrix} \cos\theta & -\sin\theta \\ \sin\theta & \cos\theta \end{bmatrix} \tag{3.8}$$

is used to determine the force exerted on the beam using equation (3.9),

$$F = R^{-1}K'R\,x \tag{3.9}$$

Θ is depicted in Figure 3.2 and calculated using the relative displacements, Δy and Δx, of M_1 from the horizontal ground surface in a trigonometric operation. In later simulations such as that depicted in Figure 3.1, Θ is calculated using the relative displacements of M_1 and M_2.

Figure 3.3 depicts the horizontal motion dynamics of the fixed beam analysis as well as the resulting forces acting on M1. Note the parameters in this simulation contain slight variations to those previously mentioned. A horizontal force in the direction opposite of slip is present and validates the expectations of generating some horizontal movement and forces in addition to vertical forces. This phenomenon is due to the directional compliancy of the beam. Although the displacement is marginal, the dynamics of the system are understood enough to pursue the next step in the simulation process.

This phenomena could have a potential to reduce slip by enacting the force on the user's foot in the direction opposite to slip. However, this will be difficult as the scenario uses a fixed beam model, which is different from the model of Figure 1.1 that has both beam ends free to move with respect to the masses. M1 is much greater than M2, and during bladder deflation, friction forces between M2 and the ground are much lower due to M1 being in a near free-fall state. Therefore, deflection during bladder collapse would simply push M2 forward (positive x direction) rather than experience significant backward (negative x direction) displacement.

The model does not yet incorporate the complexity of the slipping phenomena such as the effects of friction as one end of the beam is still fixed. This concept is explored in the following section.

a)

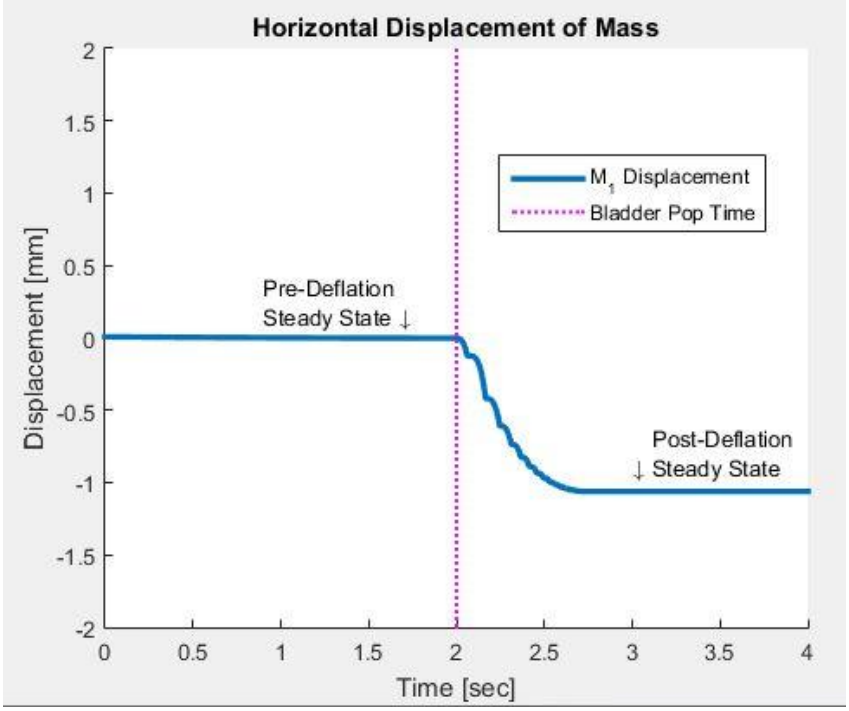

b)

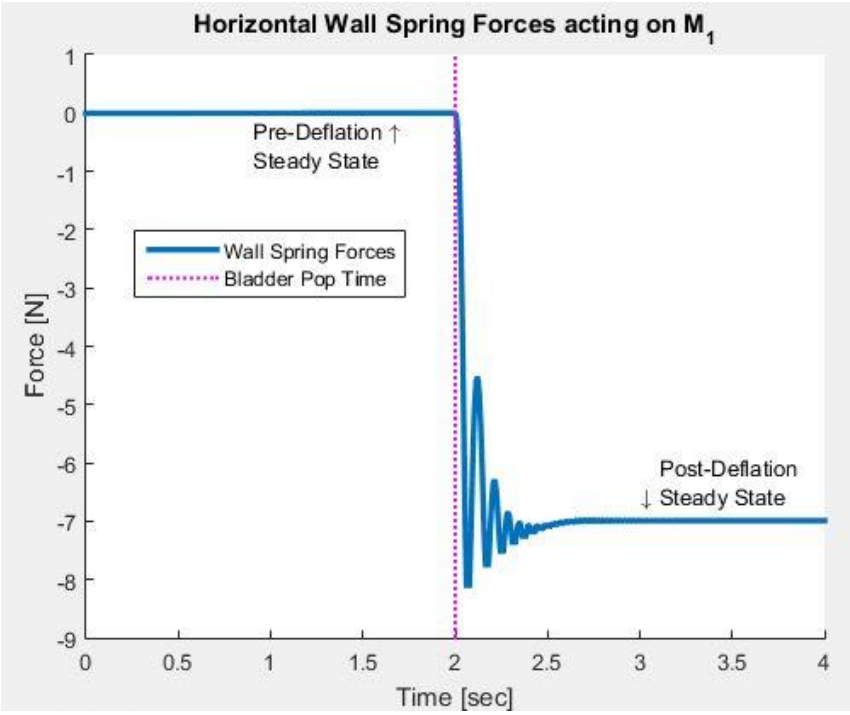

Figure 3.3: Displacement results of M_1 from fixed beam model and resultant wall spring forces.

Nonlinear Beam Structure Model

The beam model equations above describe the beam dynamics assuming a linear spring constant and a post-buckled scenario. However, it was desirous to incorporate a model that also accounts for possible scenarios of the beams in tension and when the bladders had collapsed on themselves. Therefore, a nonlinear force vs. displacement profile for the beam was created for the simulation to account for *K*, in these non-post-buckled scenarios.

The dynamics of the nonlinear model dictate that while M_1 is collapsing, the beams would experience a linear spring force dictated by equation (3.3), but once the beams had collapsed on themselves, the spring force would change to no longer reflect a beam model and would be considered a solid spring in compression using equation (3.10). The linear approximation is determined to be fairly accurate through empirical testing in Chapter 4. The same equation and values would apply for a scenario of the beams in tension.

In equation (3.10), *E* is again the modulus of elasticity, *A* is the cross-sectional area of the spring, and *L* is the thickness of the spring. Figure 3.4 depicts a simple schematic of the beams after full bladder deflation and shows how the bladder walls would begin to resemble a flat solid spring instead of collapsing beams.

$$K = \frac{EA}{L} \tag{3.10}$$

To generate a force vs. displacement curve to represent the characteristics of Figure 3.4, a region of max compression, arbitrarily chosen as 90% of the length of the beam, was specified as the point when the beam would change from the post-buckled equation (3.3) to the solid spring equation (3.10). The scenario of tension was created when the displacement of the beam was positive. However, these transition points are discontinuous and proved to be a cause of undesirable chattering when simulated. To counter this behavior, an arbitrary, small, circular curve was fitted at these points, tangent to the discontinuous profiles, to facilitate a realistically

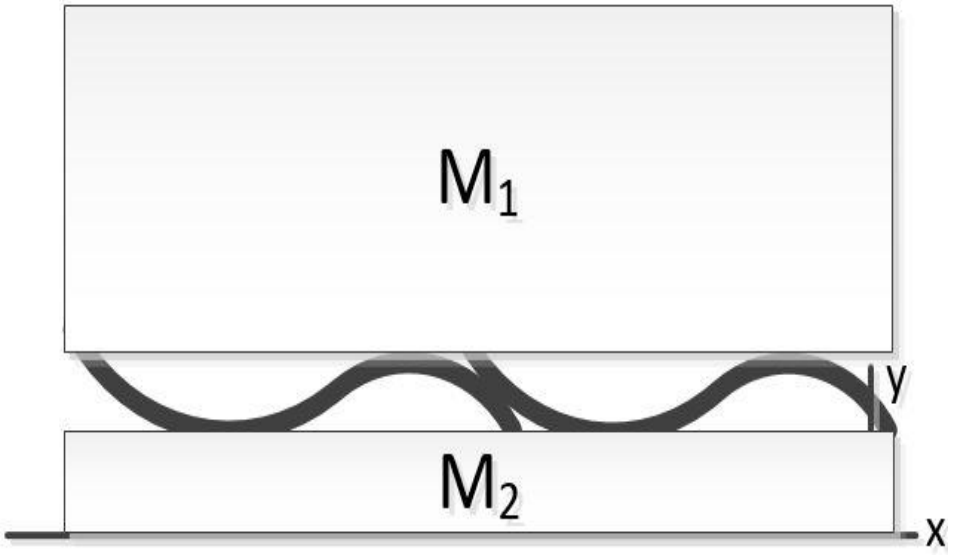

Figure 3.4: Schematic of bladder walls in collapsed position.

smooth transition from one force curve to another. When the circular curve still proved to have too much chatter, the circle feature was replaced with an elliptical curve and the chattering was mitigated. Figure 3.5 depicts the discontinuous curve, max compression region, point of tension transition, and elliptical transition curves. The values *a*, *b*, *p1*, and *q1* on the figure represent references in relation to the construction of the elliptical features and points of tangency to the discontinuous function.

Coulomb Friction Model

In order to design an accurate simulation of a slipping shoe, the beam in Figure 3.2 will be attached to a tread on the bottom of the shoe that will slide across a horizontal surface while experiencing damping and Coulomb friction. Coulomb friction was chosen to model the friction forces because of its simplicity and standard usage in many scholarly articles related to slip. It should be noted, however, that other friction models exist with the ability to analyze a more

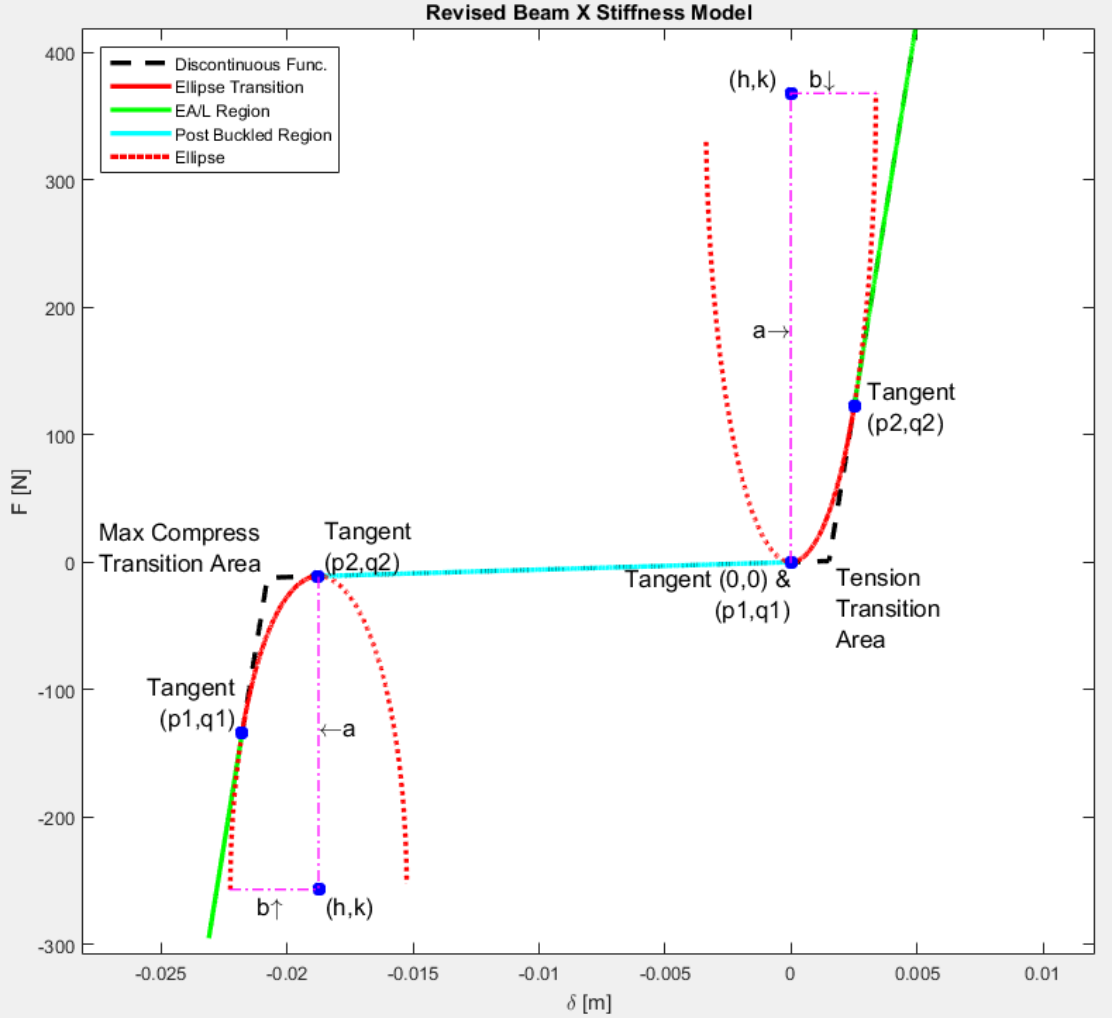

Figure 3.5: Nonlinear force vs. displacement curve for preliminary contact modeling experiments. Note that the figure was generated for beam lengths of about 20 mm.

detailed response of friction behavior. One such model, developed by P.R. Dahl, is very similar to the Coulomb model with the exception of a slight lag in friction force during directional changes [31] [32]. Other friction models often incorporate the Stribeck effect to account for viscous damping [33]. The LuGre and Leuven models are two examples that use the Stribeck effect while also incorporating hysteresis effects [32] [34, 35]. A more recent study attempts to apply slip modulating features of anti-lock brake systems and traction control systems (often used in the

automotive industry) to human gait applications. Future work may include a study of which friction models are best suited for the orthotic device discussed in this thesis.

To better understand the mechanics of friction and damping on the system, a separate analysis on a system with a simple one degree of freedom schematic is developed and shown in Figure 3.6. Note that *K* in this figure is the horizontal stiffness of a beam, to simulate horizontal motion as opposed to equation (3.1), which combines horizontal and vertical deflections. The goals of this simulation are to develop an accurate model of Coulomb friction for a mass, *M*, sliding on a horizontal surface. The effects of viscous damping from the spring and ground are neglected. To simulate friction in an iterative approach, a simple model of a mass and fixed spring is first simulated using MATLAB Simulink and shown visually in Figure 3.6. Figure 3.7 depicts the free body diagram (FBD) of *M*.

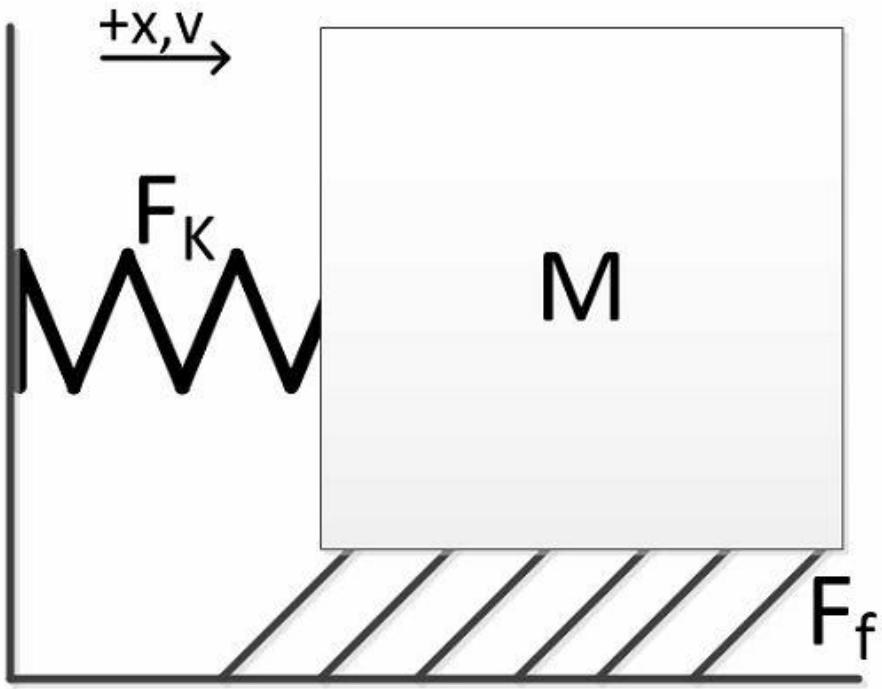

Figure 3.6: One DOF system diagram of Coulomb friction and damping.

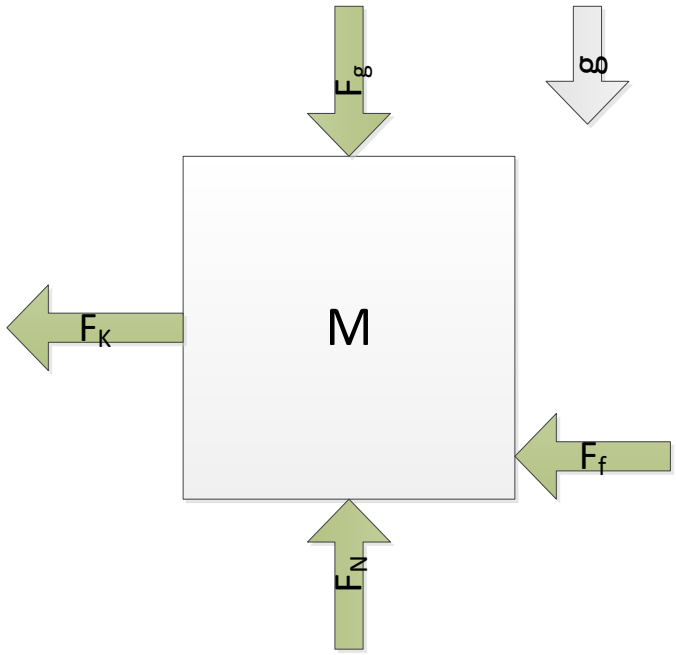

Figure 3.7: FBD for first one DOF system of Coulomb friction and damping. Note schematic is shown with spring in tension and mass moving in the positive x direction as denoted in Figure 3.8.

F_g is the weight of the mass due to g, F_N is the normal force from the horizontal surface, F_K is the force due to the spring, and F_f is the force of friction. The simulation follows equation (3.5) in a one-dimensional setting without a damping term. K and M are chosen arbitrarily while F_f is calculated using equation (1.3) and substituting F_{fmax} for F_f. Equation (1.3) is accurate for describing Coulomb friction for the system when the velocity $|v_x| > 0$. Given the importance of friction in the overall goal of a slip-preventing shoe sole, it is necessary to develop a friction model that would accurately describe the force of friction when the shoe, or mass in the case of Figure 3.6, came to a stop. Using MATLAB Simulink, a friction force decision tree has been developed to govern the system when $|v| > 0$ and when $v \approx 0$. Figure 3.8 illustrates the decision tree. Note that the decision tree uses F_f as the force of friction, μ as the friction coefficient, and F_{fmax} as the maximum possible friction force between the mass and the ground. F_{fmax} is the

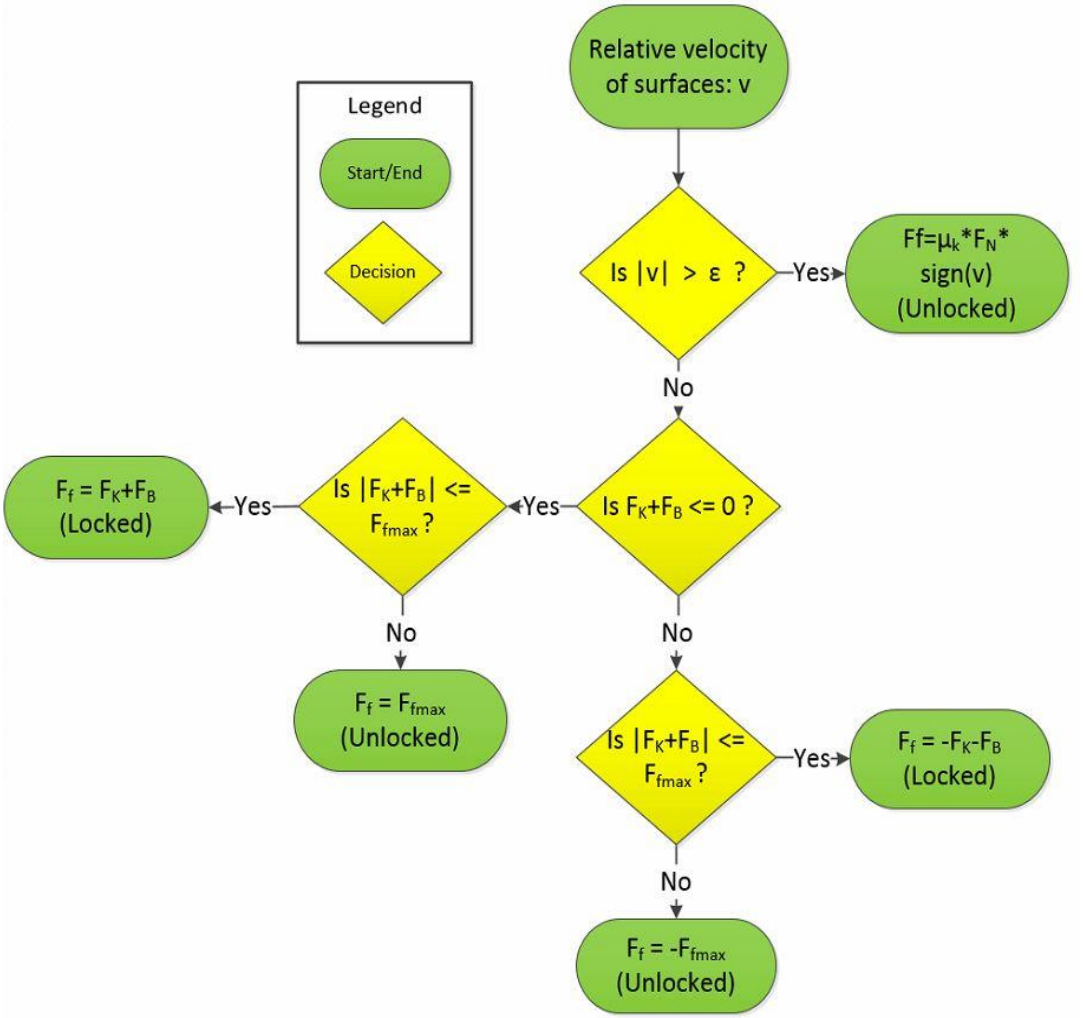

Figure 3.8. Coulomb friction decision tree for simulations.

maximum amount of friction the surface can provide using a static coefficient of friction. Note that the first decision bubble utilizes μ_k or the kinetic coefficient of friction because the mass is still moving, whereas μ_s will be used when the mass has come close to a stop. Due to the process of numerical methods, it is unlikely that v would ever exactly equal 0. Therefore, a small threshold value ε was used so that $|v| < \varepsilon$ constituted the mass coming to a complete stop. This methodology is used in other friction models discussed in Chapter 2.

Without this condition, the simulation would rarely, if ever, execute code other than that of equation (1.3). This would cause error within the simulation by preventing the block from ever reaching a “locked” state or state of stiction, as mathematically described in Figure 3.8. This locked state can occur outside the equilibrium position of the spring when the force of the spring is equal to that of the forces of friction and damping (if damping were present), thereby locking the model in a secondary state of equilibrium. Accurately describing this “locking” phenomena is important to the simulation goals as it represents when, where, or if the person has stopped slipping.

The model outlined in Figure 3.8 begins by examining the velocity of the mass relative to the ground surface. If the velocity is greater than the small threshold value, the friction is easily determined using equation (1.3). If the relative velocity is less than the small threshold value, the summation of the forces is then considered to determine whether the forces are acting positively or negatively on the mass. Once determined, the summation of the horizontal spring and damping forces is then compared to the maximum possible friction the surface can provide. If the summation is less than the maximum possible friction, the mass reaches a locked state or a state where the velocity is held at 0. If the summation is greater than the maximum possible friction, the mass is in an unlocked state or is about to gain velocity due to the acting forces. This switching between locked and unlocked states, or stiction and non-stiction states, accurately reflects the basic Coulomb friction model by allowing the nonlinearities to exist within the system without disrupting the simulation solving capabilities. One major assumption of this methodology is the value at which ε is given. This value is often difficult to decide and is application specific.

The use of the threshold value ε is imperative in this type of simulation as, noted previously, it is rare that a simulation will ever truly reach a zero-value due to the nature of

computational arithmetic. If the ε value were not used, simulation drift would occur and a state of stiction could never be reached. This concept is illustrated in Figure 3.9, which shows the simulation with and without the ε value and demonstrates the undesirable behavior of simulation drift.

Upon satisfactory results from the friction simulation depicted in Figure 3.6, the friction model has been applied to a more complex scenario shown in Figure 3.10. Figure 3.11 depicts the FBD of the shoe mass M_2. In the simulation, M_1, which represents the person, is 70 kg or roughly equivalent to a 155 lb. human. M_2, which represents the sole, is 0.5 kg or about 1 lb.

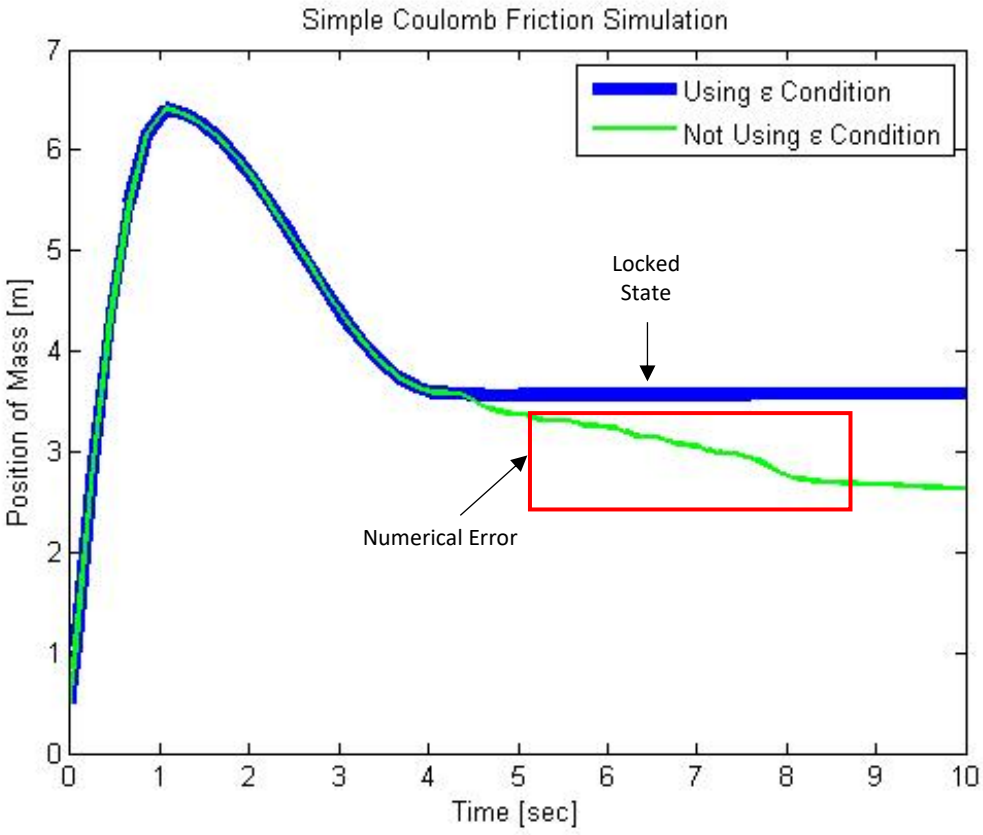

Figure 3.9: Results of one DOF simulation
with and without the ε condition.

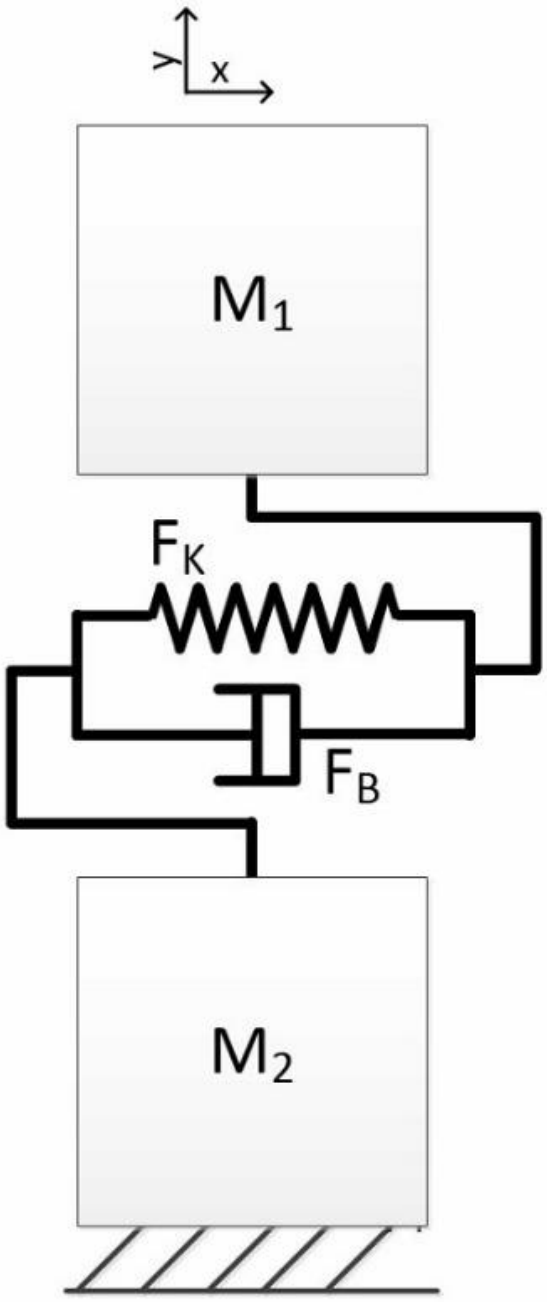

Figure 3.10: Second version of system representing human and shoe relationship.

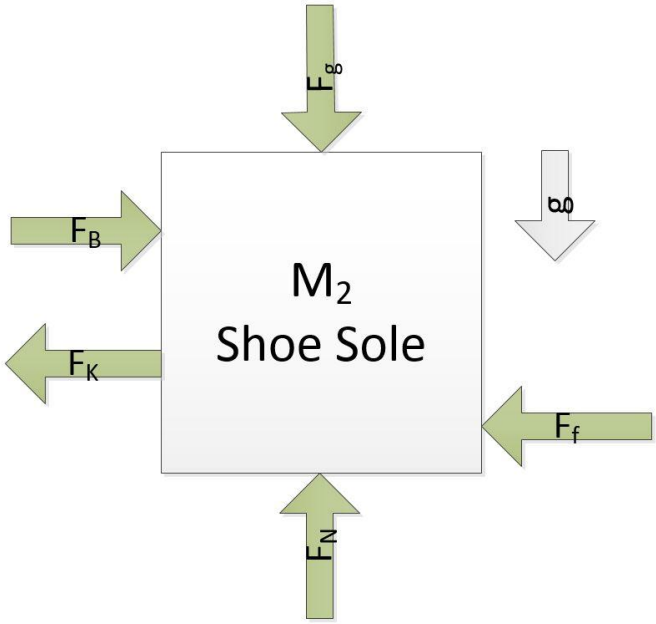

Figure 3.11: FDB of M_2 from the ideal schematic or the shoe sole mass that will be simulated at a later time.

For this simulation, it is assumed that the F_N acting on M_2 should account for the combined weight of both masses to more accurately predict how the proposed orthotic device might function in a friction model scenario. The following figures demonstrate the results of the simulation for M_1 and M_2. Figure 3.12 represents the position of each mass with respect to time as well as the positional difference.

The simulation represents the expected response with the shoe sole mass moving until stopped by frictional forces and the person mass moving a farther distance before returning to a steady state position with the shoe sole. When given an initial velocity, the masses undergo a small amount of relative translation followed by a steady state value of no relative translation. The results are valuable because they represent the user's ability to maintain balance while slipping. The greater X_1-X_2 (horizontal distance between M_1 and M_2) becomes, the more movement the person will feel with respect to the shoe and the more difficult balance will be to

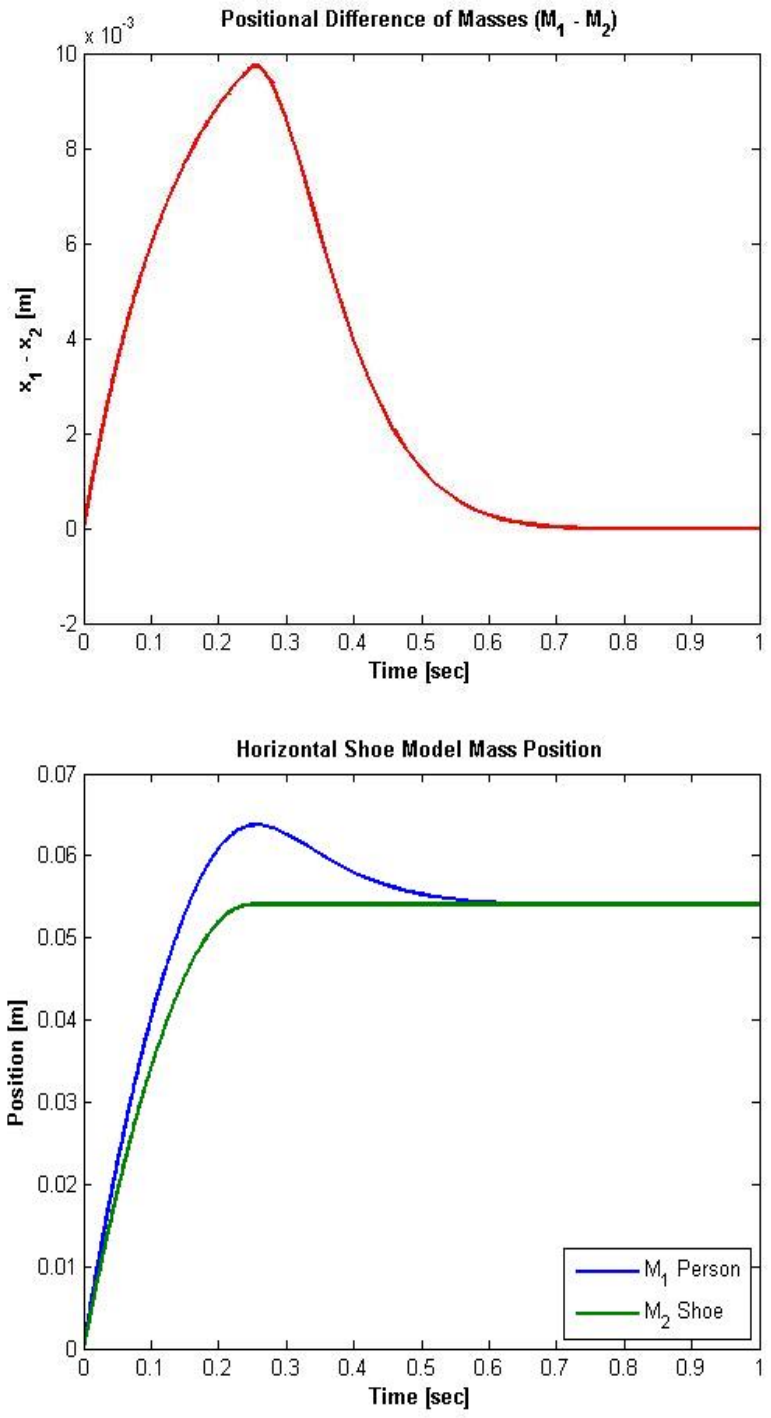

Figure 3.12: Horizontal Shoe Model simulation positional results.

achieve. The displacement between the two masses is due to the compliance of the spring allowing the masses to slip at differing relative velocities. The various forces acting on the system are also of interest to us as modeling friction and damping is a large part of the simulation development process. Figure 3.13 illustrates the various forces acting on the two masses, which behave as expected.

The results in Figure 3.13 are exciting because they show the friction model behaving without noise distortion typical of transition between slip and stick modes. The friction is shown to be steady while the system is in motion until stiction is beginning to be achieved where it becomes a function of the spring and damping forces. All forces go to a steady state value once the masses have come to rest and the spring has reached an equilibrium. Once the velocity of M_2 has reached a locked state, we see the friction model represents the numerical opposite of the spring and damping force summation. Eventually, the forces correctly reach a steady state of zero in harmony with the timing of Figure 3.12.

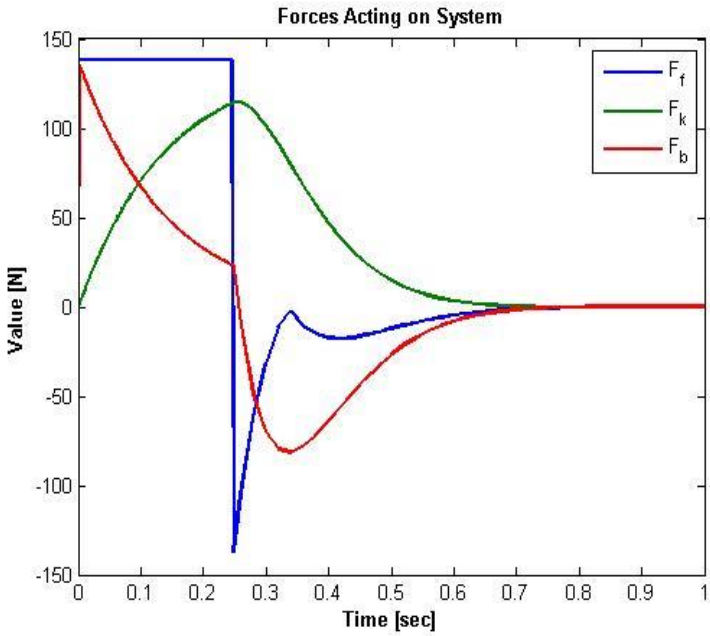

Figure 3.13: Various forces acting the Horizontal Shoe Model system.

During simulation of the model discussed at the end of this chapter, it was found that M_1 tended to drift once the system came to rest. This drift is attributed to relative motion between the top and bottom surfaces of the orthotic device, or between M_1 and M_2 of the simulation. In the context of the shoe slip scenario discussed throughout this thesis, contact between the masses is a major element to the overall model. Therefore, some friction between the two mass surfaces will exist. To account for this undesirable drift behavior in a manner most expected to resemble the orthotic device in action, a second Coulombic friction element was added in the horizontal direction between the top and bottom surfaces of the orthotic device bladders. Schematically, this is akin to adding a second friction element between M_1 and M_2 in Figure 3.10. The second friction model followed the same logic outlined in Figure 3.8, however, when locking or stiction occurs between M_1 and M_2, M_1 does not stop moving or hold position in the horizontal direction. Instead, the horizontal position and velocity of M_1 becomes entirely dependent on M_2, or in other words, the horizontal velocity of the two masses are equal. This is analogous to stiction between the ground surface and M_2. Note that spring and damper forces between the two masses are still in effect. The following table contains state equations outlining the horizontal kinematics of M_1 and M_2. To differentiate between the surfaces in Table 3.1, let Surface A represent the surface between M_1 and M_2 and Surface B represent the surface between M_2 and the ground. Also note that $^{(-)}$ denotes the value calculated one time step previous to the time step when stiction first occurred. Upon resimulation, the drifting phenomena in M_1 was no longer observed.

To simulate friction between the top and bottom of the orthotic device bladders, a COF between the two surfaces of the *Mold Max* [30] material needed to be determined. This was performed via a simple test depicted in Figure 3.14. Two sheets of the rubber *Mold Max* material (a) were molded and adhesively attached to two boards (b). The rubber surfaces were

Table 3.1: State variables during stiction and non-stiction events for Surfaces A & B.

State Variable	$t_{stiction}$	$t \neq t_{stiction}$
x_1 **Surface A**	$(x_1 - x_2)^{(-)} + x_2$	x_1
$\dot{x_1}$ **Surface A**	$\dot{x_2}$	$\dot{x_1}$
x_2 **Surface B**	$x_2{}^{(-)}$	x_2
$\dot{x_2}$ **Surface B**	0	$\dot{x_2}$

then placed atop one another with handheld weights (c) stacked on the boards. The bottom board is rigidly attached to the force plate of the Ankle Foot Simulator (AFS) [36] force plate (d).

The use of the AFS is discussed further in Chapter 4. Using a smooth pulley (e) with minimal friction, a rope (f) was attached to the moving board and was pulled by hand through the pulley while the normal forces and horizontal forces were recorded by the force plate. The test was performed using 10 lb and 20 lb handheld weights.

Figure 3.15 displays a sample output of the test using 10 lb weights. The data show an initial spike in COF, which was assumed to be the static COF, followed by a dip before increasing again. The dip was considered as the kinetic COF and the following rise in COF was attributed to be viscous forces. These values for COF are utilized in the final simulations discussed at the end of this chapter. The test utilizing the 20 lb weights showed similar results.

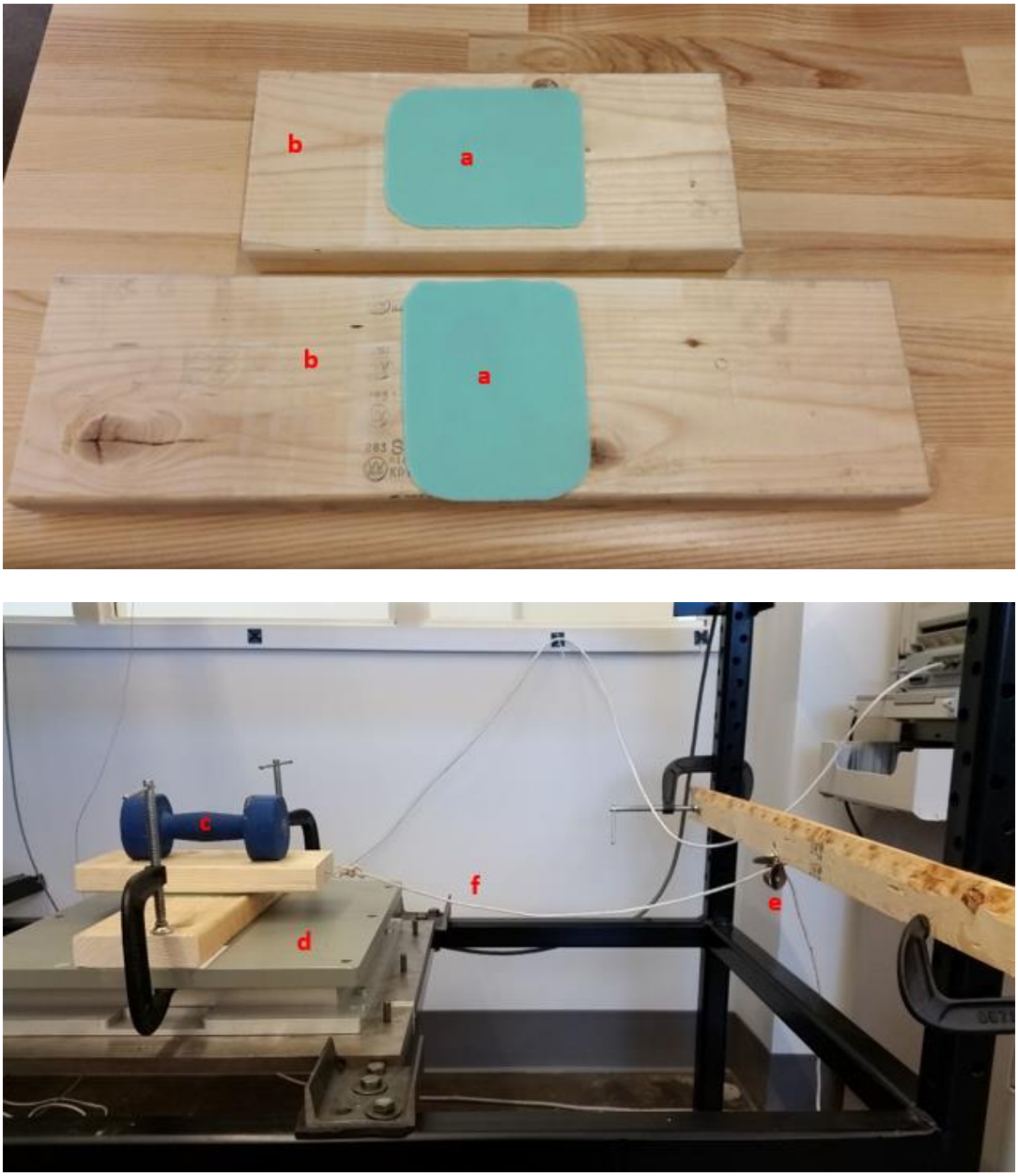

Figure 3.14: Test set-up for Mold Max on Mold Max rubber COF test. a) Molded rubber sheets. (b) Boards with rubber adhesively attached. (c) Handheld weights used as downward force to generate larger friction forces. (d) AFS force plate. (e) Smooth, low friction pulley. (f) Rope used to create relative motion between rubber surfaces.

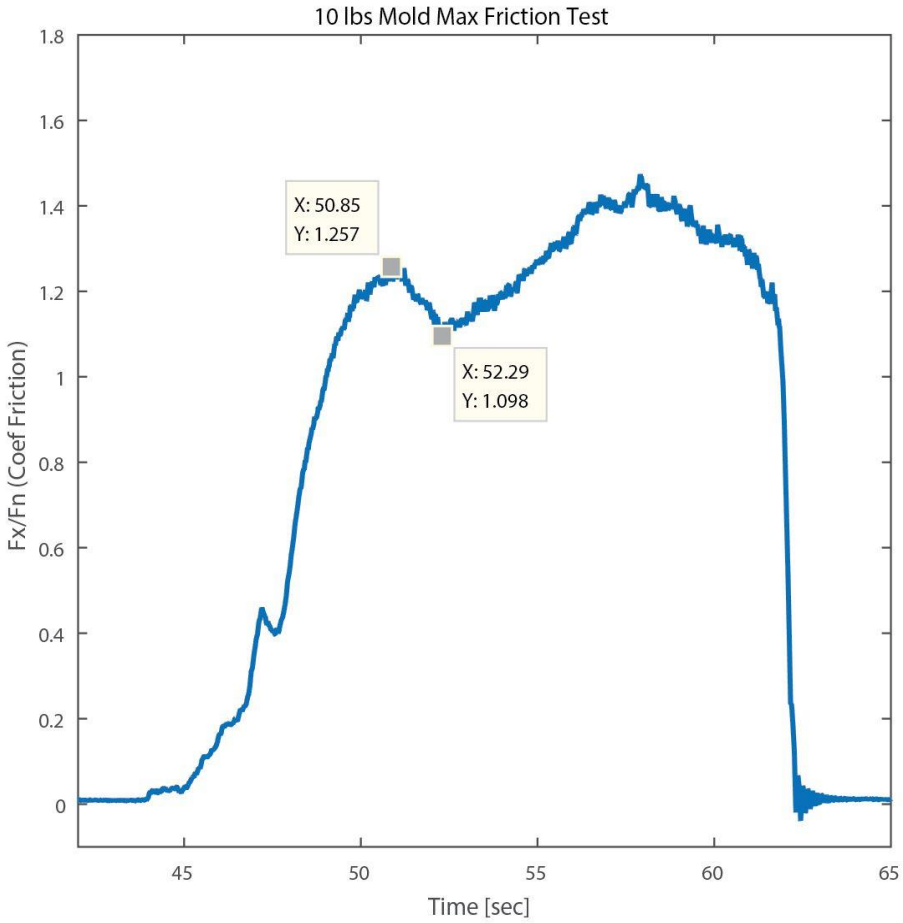

Figure 3.15: Results of Mold Max friction test using 10 lbs. First highlighted point is assumed to be static COF and second highlighted point is assumed to be the kinetic COF.

Air Flow Model

A preliminary attempt to understanding air flow dynamics of the proposed orthotic device schematic shown in Figure 1.1 was conducted in this study. Many of the assumptions in this thesis assume that flow resistance in the bladder valves will be negligible, which imply a quick collision of the user's foot with the ground or bottom of the orthotic device. Therefore, an attempt to model the air flow through the valve system as the bladders are deflating was developed. The purpose of the model was to gain an understanding of the flow rate and its effect on impact forces.

Preliminary attempts to model the system assume a piston cylinder structure of the bladders under Ideal Gas Law (IGL) conditions and experiencing four sources of flow rate restriction. The IGL is shown in equation (3.11) where *P* is pressure in the cylinder, *V* is the volume of the cylinder, *n* is the amount of air in the cylinder in moles, *R* is a constant, and *T* is the temperature of the gas in Kelvin units.

$$PV = nRT \tag{3.11}$$

Figure 3.16 depicts the simplified schematic of the bladder and valve system model. Figure 3.17 depicts a schematic of the sources of resistance in the valve system.

The air enters the valve system through a small orifice, passes through the mechanical valve, and exits the valve through another small orifice into a smooth tube before exiting to atmosphere. Note that the flow restrictions in the orifices in modern fluid dynamics are considered minor losses, and therefore were not considered in the model. Therefore, the model shown in Figure 3.17 is for reference only.

The valve resistance is specified by the manufacturer [37] and was assumed to be in the subsonic flow range. This was determined through a rough calculation of hypothetical weight due to gravity generated by M_1 and divided by the area of the bladder surface. The flow rate equation used for the valve is shown as equation (3.12) where *Q* is the flow, *K* is a gas units constant specified by the manufacturer, f_T is a temperature correction factor specified by the manufacturer, *P* is the pressure, and *Lohms* is a resistance value specified by the manufacturer.

$$Lohms = \frac{2Kf_T\sqrt{(P_2 - P_3)\,P_3}}{Q} \tag{3.12}$$

The flow resistance due to the smooth tube is computed using the Darcy–Weisbach formula [38] shown in equation (3.13) where *L* is the length of the tube, *D* is the hydraulic tube diameter, *ρ* is the density of the flow medium, *A* is the cross-sectional area of the tube, and *f* is the Darcy friction factor coefficient.

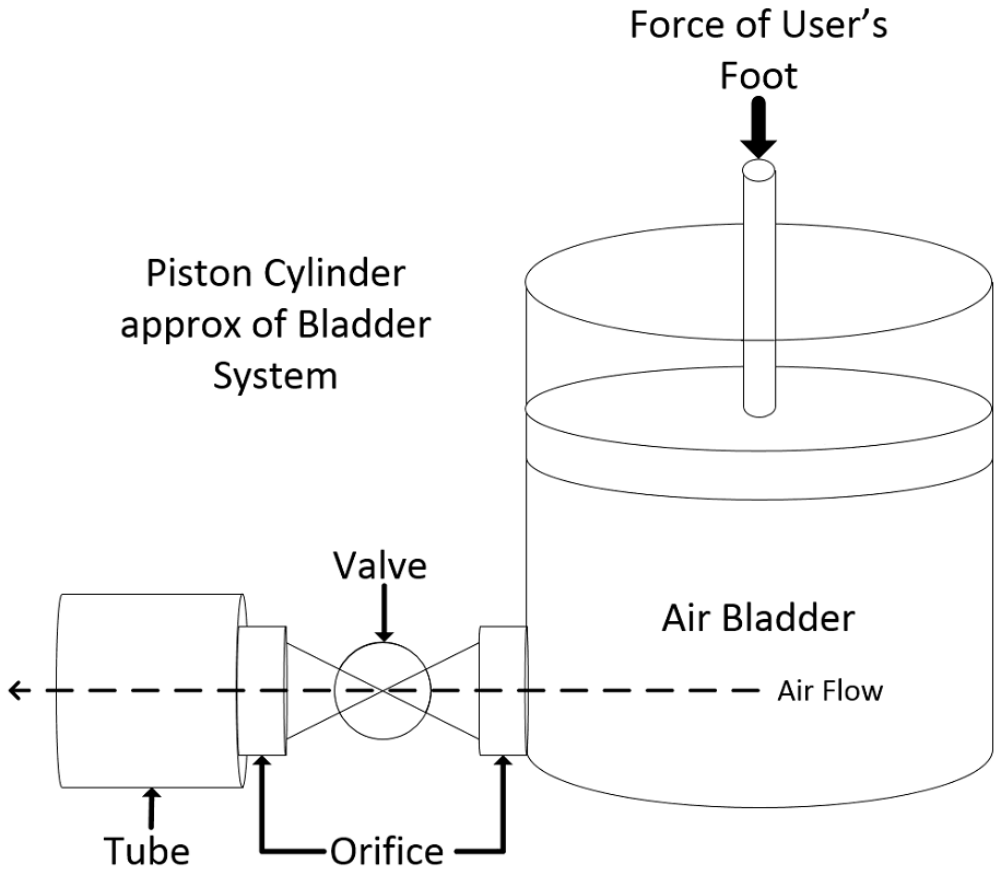

Figure 3.16: Simplified schematic of air bladder and valve model.

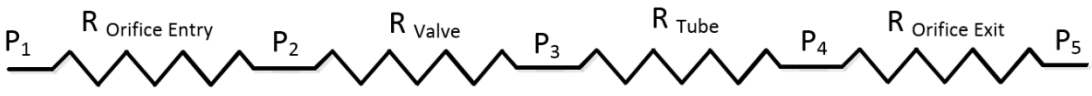

Figure 3.17: Diagram of sources of flow resistance in preliminary air flow model.

$$P_3 - P_4 = f\frac{L}{D}\rho\frac{Q^2}{2A^2} \tag{3.13}$$

Since P_2 can be considered the pressure inside the cylinder solved using the IGL and P_4 is atmospheric pressure, P_3 is an unknown variable common in both equations. Therefore, the equations can be combined into equation (3.14) and solved for Q.

$$Q = \frac{2}{R}\left[\frac{P1fL\rho Q^2}{2DA^2} + P_2P_4 - \left(\frac{fL\rho Q^2}{2DA^2} + P_4\right)^2\right]^{1/2} \tag{3.14}$$

The remaining unknown variable is f, which is normally solved by numerical methods using the Colebrook formula [39] shown in equation (3.15) where R_e is the Reynolds number and ϵ is a measure of the effective roughness height of the tube. However, the Colebrook formula cannot be solved for f explicitly and therefore cannot be substituted into equation (3.14). To approximate f, the Haaland formula [40], shown in equation (3.16), is used that approximates the Colebrook equation within a marginal amount of error under certain flow rate limits.

$$\frac{1}{\sqrt{f}} = -2\log\left(\frac{\epsilon}{3.7D} + \frac{2.51}{R_e\sqrt{f}}\right) \tag{3.15}$$

$$f = \left\{-1.8\log\left(\left[\frac{\epsilon/D}{3.7}\right]^{1.11} + \frac{6.9\nu A}{QD}\right)\right\}^{-2} \tag{3.16}$$

For simplicity, the following substitutions are made.

$$a = \frac{L\rho\left\{-1.8\log\left(\left[\frac{\epsilon/D}{3.7}\right]^{1.11} + \frac{6.9\nu A}{QD}\right)\right\}^{-2}}{2DA^2} \tag{3.17}$$

$$R = \frac{Lohms}{Kf_T} \tag{3.18}$$

Finally, equation (3.19) is formed and provides a numerical method approach to calculate flow rate between P_2 and P_4. Q is solved using a nonlinear root solver in MATLAB. A state variable, n, for the number of moles is added to the simulation and varied based upon flow rate Q. The

remaining number of moles is then used to calculate the force exerted by the bladder system via equation (3.11).

$$0 = a^2Q^4 + \left(\frac{R^2}{4} + 2P_4a - P_2a\right)Q^2 + \left({P_4}^2 - P_2P_4\right) \tag{3.19}$$

Equation (3.19) was simulated under the schematic shown in Figure 3.1. The schematic assumes the air model acts analogous to a vertical spring between M_1 and M_2. Figure 3.18 depicts a sample output of the number of moles from the simulation as well as the force generated by the air model.

To determine turbulence of the predicted flow, equation (3.20) was used to calculate the Reynolds Number (R_e) where *u* is the average velocity of the air flow, *v* is the kinematic viscosity, and *d* is the tube diameter. The kinematic viscosity used for the simulation was: $v = 1.568 * 10^{-5}$ [41]. The Reynolds number is approximately $R_e = 2006$, which shows the flow to be in the transition range from laminar flow. This suggests a possible source of error in the flow models as the Darcy–Weisbach equation utilized in this thesis conservatively assumes turbulent flow.

$$R_e = \frac{ud}{v} \tag{3.20}$$

Numerical parameters for the tests are discussed in the Combined Models section at the end of this chapter. The simulation shows the bladder valves actuating at roughly 19 seconds and emptying in roughly 400 ms. As a metric to provide a rough comparison of this flow rate, the deflation time is compared to the time it takes for a mass to free fall from a similar height.

Equation (3.21) can be used to determine a free fall time for a mass dropped from a height with zero initial velocity and neglecting air resistance. In this equation, *d* is the free fall distance, *g* is the acceleration due to gravity, and *t* is the time for free fall. Using these

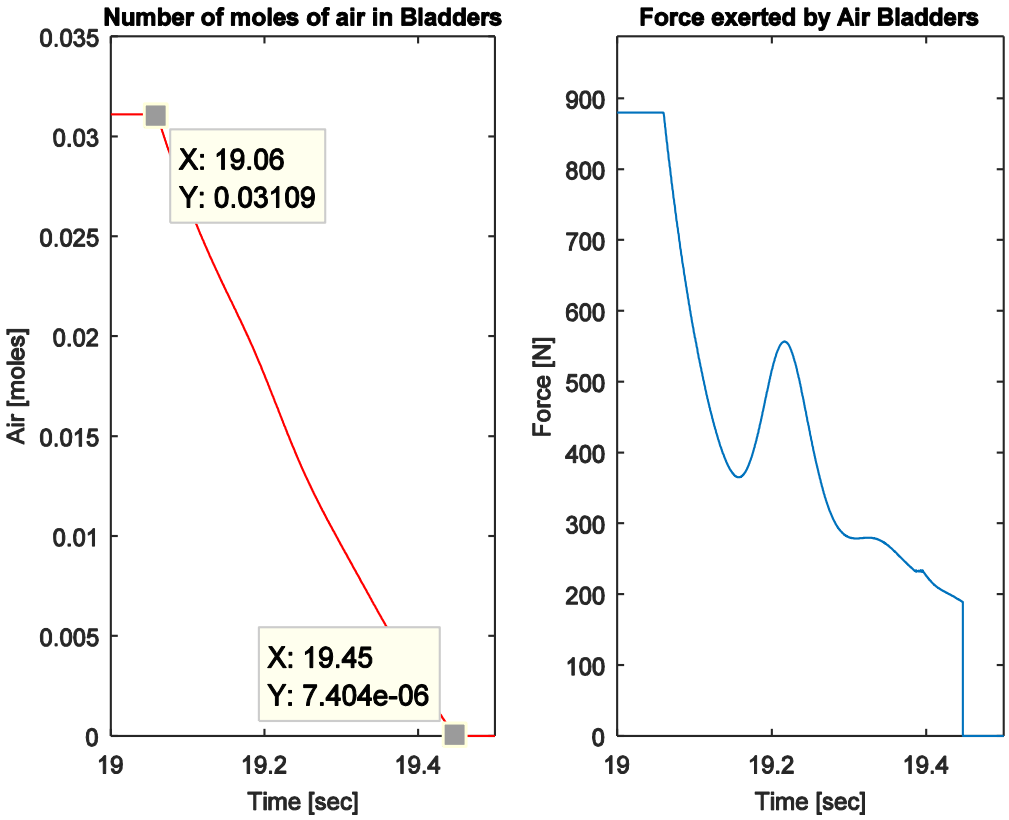

Figure 3.18: Simulation sample air model output.

parameters, the fall time is about 90 ms, which leaves roughly 300 ms due to flow resistance in the system.

It is desirable for the user's foot to experience a deflation time near that of free fall in order to generate the largest possible impulse. This simulation appears to identify one limiting factor for the orthotic device and should be considered carefully in future designs. The amount of flow resistance, which is caused by the bladder wall forces and valve flow resistance, are further explored in Chapter 4 during the empirical testing of the Air Flow Model and Bladder Beam Models. During this testing, it is shown that the valves contribute the majority of the flow resistance.

$$\sqrt{\frac{2d}{g}} = t \tag{3.21}$$

In order to estimate the flow rate that would be required for negligible flow resistance during deflation time, several simulations were tested that multiplied the flow rate shown in Figure 3.18. Figure 3.19 shows the simulation results that predict that a flow rate 5 times greater than what is currently used on the orthotic device prototype (described in Chapter 4) would be needed in order to reach a near free fall deflation time of 90 ms mentioned above.

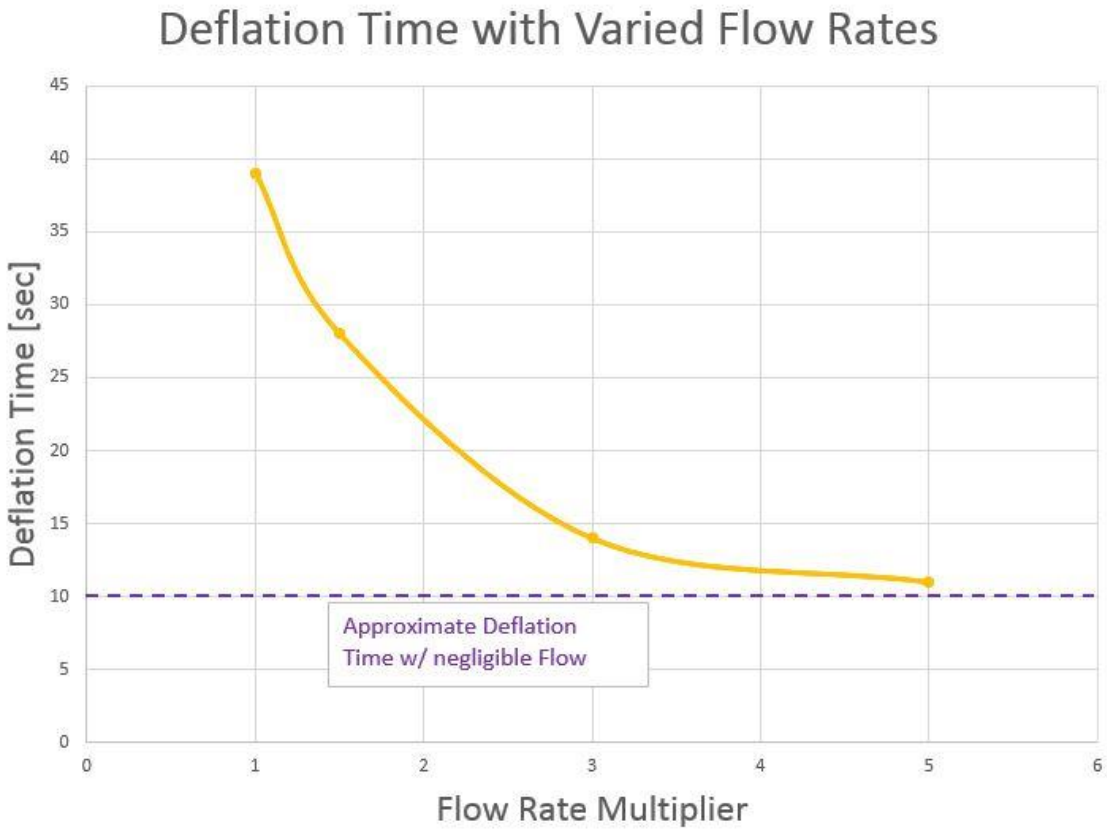

Figure 3.19: Flow rate required to reach negligible flow resistance so that bladders collapse at a near free fall time of 90 ms. A flow rate multiplier of 1 denotes the current valve system used for the prototype discussed in Chapter 4.

Contact Modeling

Since contact with the ground plays a large effect in equation (1.5) and in the proposed orthotic shoe device, various contact models were simulated in an attempt to predict N_i. Several factors play a role in effective contact modeling such as the type of material that will experience the contact forces. The current proposed *Mold Max* [30] material, or others similar in shoe structure, utilize compliant rubbery materials that tend to dissipate energy effectively. Therefore, contact equations such as those of equations (2.1) and (2.2), are not ideal for predicting N_i for the scenarios proposed in this thesis because of the lack of energy dissipative features.

To better understand contact equations and the effectiveness in dynamic simulations, an iterative approach to contact modeling was undertaken. First attempts studied one of the simplest forms, equation (2.2), to model the ground contact as a very stiff spring. This attempt experienced a common chattering behavior typical of simulations. Another approach explored a nonlinear spring constant analogous to the nonlinear beam model in Figure 3.5 and excluding the portion relating to tension. Figure 3.20 illustrates the nonlinear model for the ground stiffness spring.

The issues with chattering in the simulation were solved by the curve in Figure 3.20; however, the model does not account for the energy dissipative properties common with compliant materials and is difficult to validate through empirical means. Therefore, two new contact models from published literature [23] [27], equations (2.4) and (2.5), were experimented with because of their distinct abilities to better model energy dissipative materials. In simulation, both equations produced reasonable results without the negative effects of chattering. Further testing to validate the equations would need to be performed once a prototype was constructed. Simulation outputs for these contact models are shown as

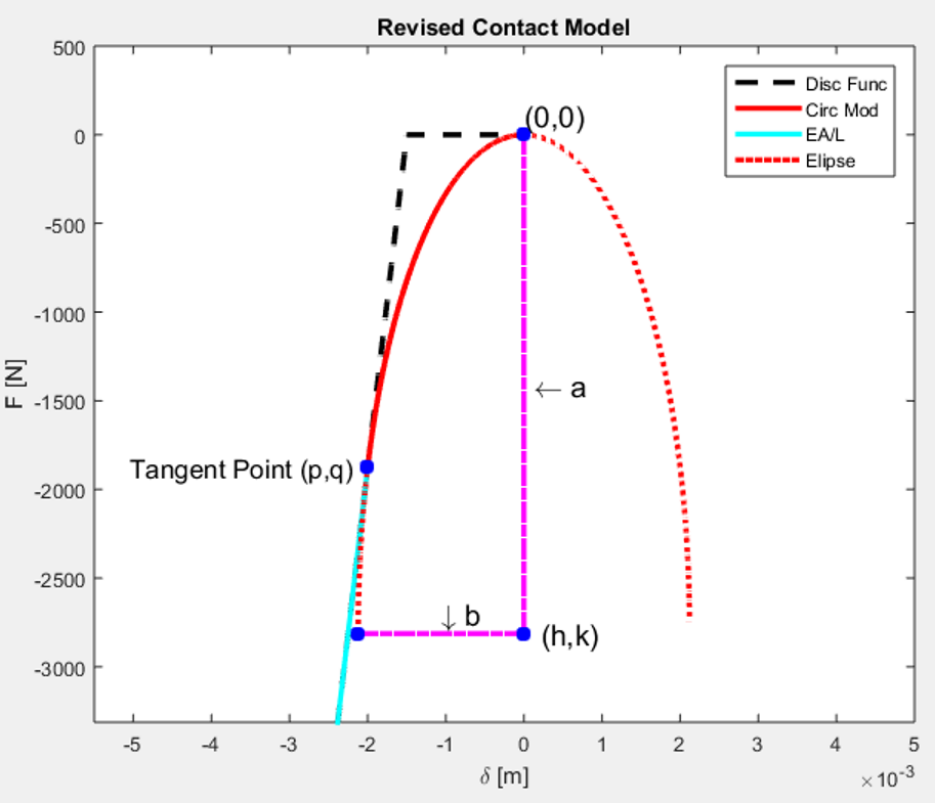

Figure 3.20: Nonlinear force vs. displacement curve for preliminary contact modeling experiments.

normal force readings resulting from the final simulation scenario and are discussed at the end of this chapter.

Coefficient of Restitution Analysis

The contact models discussed above utilize a coefficient of restitution (COR) that had yet to be determined for the orthotic device system. The material used to determine the COR for the orthotic device was chosen to be the same *Mold Max* [30] rubber material used in the bladders and shoe sole.

To determine the COR, a rubber ball was molded using a standard ping pong ball plastic housing and dropped on a solid surface of *Mold Max* material. The resulting bounce height was

recorded using a camera at 60 Frames Per Second (FPS). A resulting average COR, or *e*, was derived using equation (3.22) where v_f and v_i are the velocities of the ball just after first bounce and just before first bounce [42]. Equation (3.22) is modified using the classic equations for potential and kinetic energy, shown below as equations (3.23) and (3.24), where *m* is the mass of the object, *g* is the acceleration due to gravity, *h* is the height of the ball relative to the ground, and *v* is the collision velocity. Since Potential Energy (*PE)* and Kinetic Energy (*KE)* are equal when other energy dissipative forces are negligible, equations (3.23) and (3.24) can be rearranged to equation (3.25), which can then be substituted into equation (3.22) and simplified to create equation (3.26). This final equation utilizes h_i as the initial height and h_f as the height of first bounce, which are relatively easier values to determine empirically than velocity. Figure 3.21 shows the test set-up schematic.

$$e = \frac{v_f}{v_i} \tag{3.22}$$

$$PE = mgh \tag{3.23}$$

$$KE = \frac{1}{2}mv^2 \tag{3.24}$$

$$v = \sqrt{2gh} \tag{3.25}$$

$$e = \frac{h_f}{h_i} \tag{3.26}$$

The test was performed with two different balls at approximately three different heights, 20 mm, 40 mm, and 60 mm, with three bounces at each height. Averages and standard deviations were calculated from the data collected via video playback. Table 3.2 summarizes the results, which were close enough in average COR as well as minimal standard deviation to be counted conclusive.

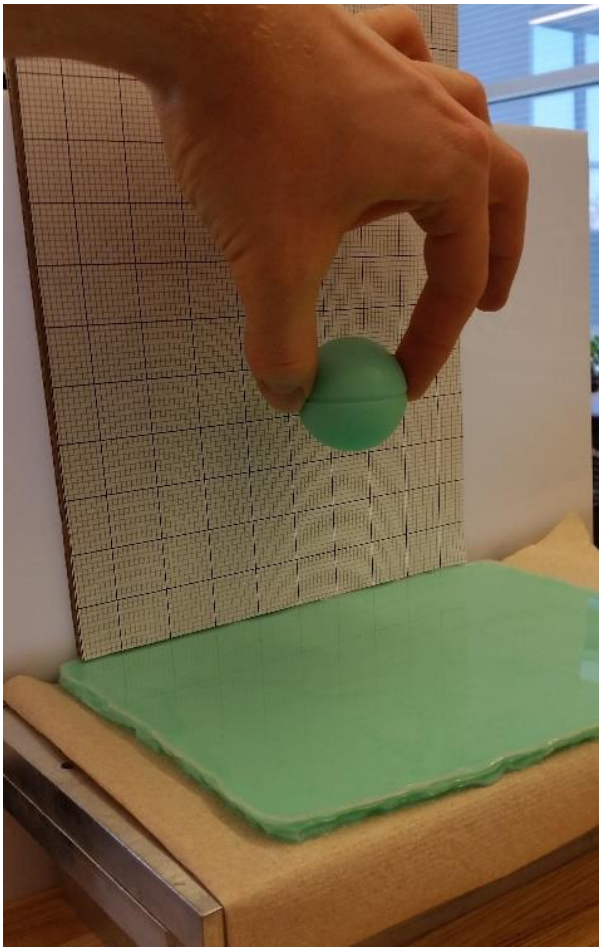

Figure 3.21: Coefficient of restitution test set-up.

Table 3.2: Major results of Coefficient of Restitution test showing the average result +/- one standard deviation.

Drop Height	20mm	40mm	60mm	**Total Avg.**
Average Coef. Rest.	0.829 ± 0.011	0.850 ± 0.009	0.848 ± 0.004	**0.842 ± 0.008**

Combined Beam, Air, Friction, and Contact Models

The previous models discussed in this thesis were combined into one lumped-parameter simulation that predicted dynamic behavior in a multiphysics scenario that is depicted in Figure 3.1. The system was then given a constant horizontal force acting on both masses to ramp up to a larger speed and then allowed to slow, due to friction, to a desired slip velocity at which to actuate the bladder valves. Two slip velocities are described in this section that demonstrate system dynamics under no-slip where $v_{slip} = 0$ m/s, and at 1 m/s. Note that in the first scenario, the system was actuated at rest and not given the constant horizontal force. When $v_{slip} = 0$ m/s, the system actuates from a steady state position and zero velocity, which provides a reference for the other results. The velocity of $v_{slip} = 1$ m/s was chosen because, at this speed, several behaviors of the simulated system can be seen. One particularly desirable behavior is seen where the bottom of the shoe sole, or M_2, experiences relative velocity with M_1. This behavior highlights how stiction between the bottom of the shoe could be achieved if the bladder system were actuated at the appropriate velocity. The other desirable behavior displayed at this speed is the ability of the impact of the two masses to generate enough friction force to slow the system to a complete stop sooner than if no actuation had occurred.

For both speeds, contact forces or normal forces are shown as well as velocity profiles. The shoe structure was chosen to roughly estimate a men's size 10.5 shoe or the average shoe size for a male in the U.S. with a simple square profile of 25 cm in length and 8 cm in width [43]. Bladder wall thickness was desired to be as thin as possible to maximize impact velocity of the user's foot without compromising future prototype structural integrity. This is assumed to be roughly 2.5 mm as per prototypes developed by Wang [2] [3]. Bladder height was desired to be as large as possible to allow more time for downward acceleration of the user's foot while maintaining some form of stability for the wearer. This value was determined as 40 mm per

testing performed by Wang [2] [3]. Bladder wall angles were also chosen to be vertical to maximize height, minimize weight of shoe, and allow similar behavior with forward and backward slip. A total of 4 bladders were used in the simulation to minimize the number of walls while also allowing the forces along the different segments of the foot to be isolated to improve stability. A kinetic COF of 0.25, determined via the testing procedures of Chapter 4, was used in the simulations below with an arbitrary static COF of 0.3.

To illustrate the simulation graphically, a movie was created in MATLAB to visualize the orthotic device in motion. Figure 3.22 provides several frames from the simulation. The plots show frames in time for the simulation at an initial position (a), after the force is removed and the bladder reaches a static deflection just prior to bladder actuation (b), as the bladder is

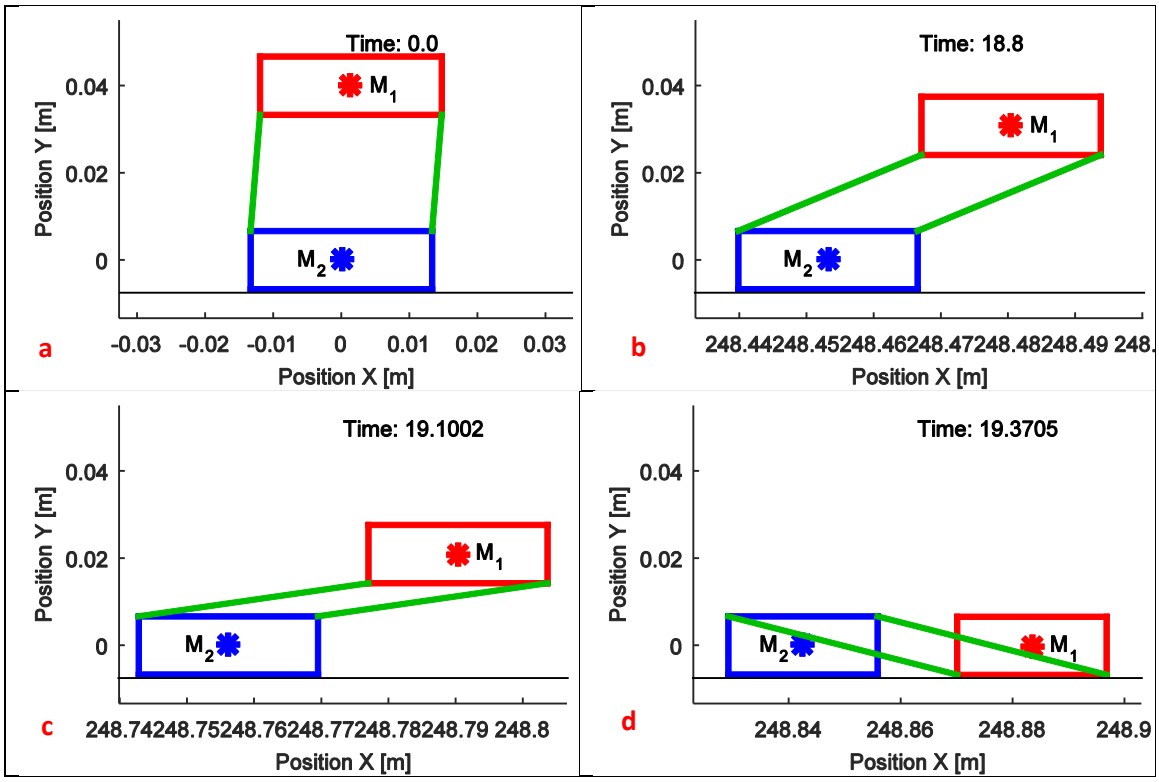

Figure 3.22 : Screenshots representing simulation values of orthotic device. a) Initial Position. b) After the force is removed and the bladders reach a steady state deflection just before actuation. Screenshots of representing simulation values of orthotic device. c) As the bladders are collapsing. d) When the system reaches equilibrium.

collapsing during deflation (c), and once the system has reached equilibrium (d). Values of wall beam forces, pressure, friction, contact, and velocity, are given in each frame. Displacements between M_1 and M_2, and overall wall length in comparison to starting values are also given. All values are in SI units.

Figure 3.23 depicts the downward velocity profile as well as the contact forces for the simulation when under zero slipping conditions (e.g., $v_{slip} = 0$). Note that actuation occurs at 4 seconds followed by a state of free fall and acceleration before making impact and a large spike in normal forces.

This spike in normal force is exciting as it demonstrates that large normal forces are achievable at relatively low heights of 40 mm off the horizontal. These large spikes will be validated later in the thesis by empirical testing and applied to equation (1.5) to analyze slip mitigating abilities.

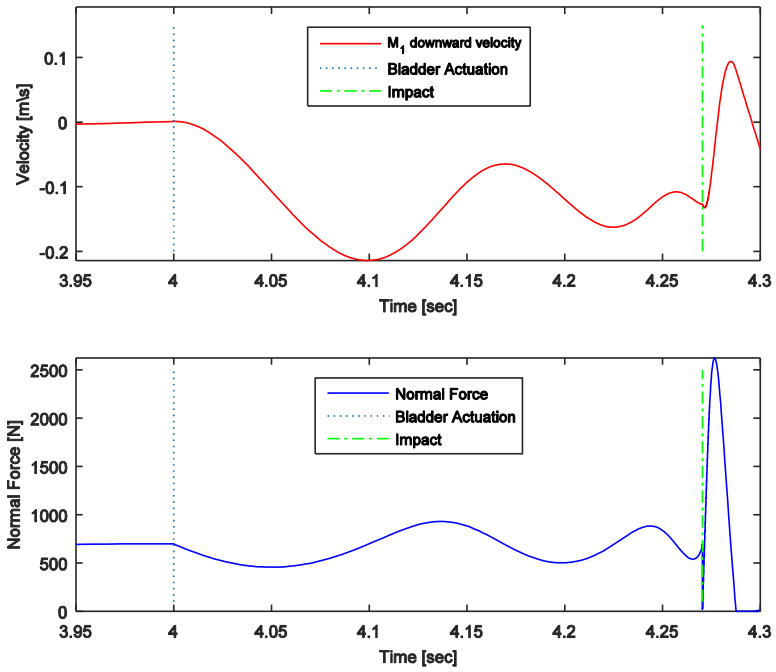

Figure 3.23: Downward Velocity profile and Normal Force profile for zero-slip (e.g., v=0) scenario in simulation.

Figure 3.24 depicts the same parameters for a simulation where the bladders are actuated at $v = 1\ m/s$ horizontal velocity as well as the horizontal velocity profiles of M_1 and M_2. Note how the relative velocity between the two masses actually shows M_2 increasing in deceleration momentarily between the actuation and impact time periods shown in Figure 3.24 before picking up speed due to the inertia of M_1 continuing to move forward. If actuated at the appropriate time, stiction could be achievable because of the directional compliance within the beam structure causing a negative force on M_2. The force would allow M_2 to momentarily travel slower than M_1.

If this relative velocity is greater than or equal to the velocity of M_1, stiction of M_2 will occur. This is an interesting and desirable behavior as stiction can be momentarily created simply with directional compliancy. However, it is also interesting to note that during this period of relative velocity, the deceleration of M_1 decreases due to M_1 being in a near free-fall type scenario.

During this time frame between bladder actuation and impact, the normal forces are only a function of the mass M_2, the force of the bladder walls, and the force exerted by M_1 to push the air out of the bladders. This force fluctuates as air is released but generally is less than the force exerted by the weight of M_1 before actuation occurs. This reduction in normal force and corresponding friction force on the system causes the deceleration of M_1 to decrease.

After impact, the results show a rapid increase in deceleration of M_1, indicating that the spike in normal force has generated significant friction forces to slow the velocity of both masses. This increase in friction force is due to the increase in normal forces caused by the impact of the masses.

Table 3.3 highlights the differences in approximate stopping time of M_1 from the scenario depicted in Figure 3.24 and how the time compares to a simulation where no bladder

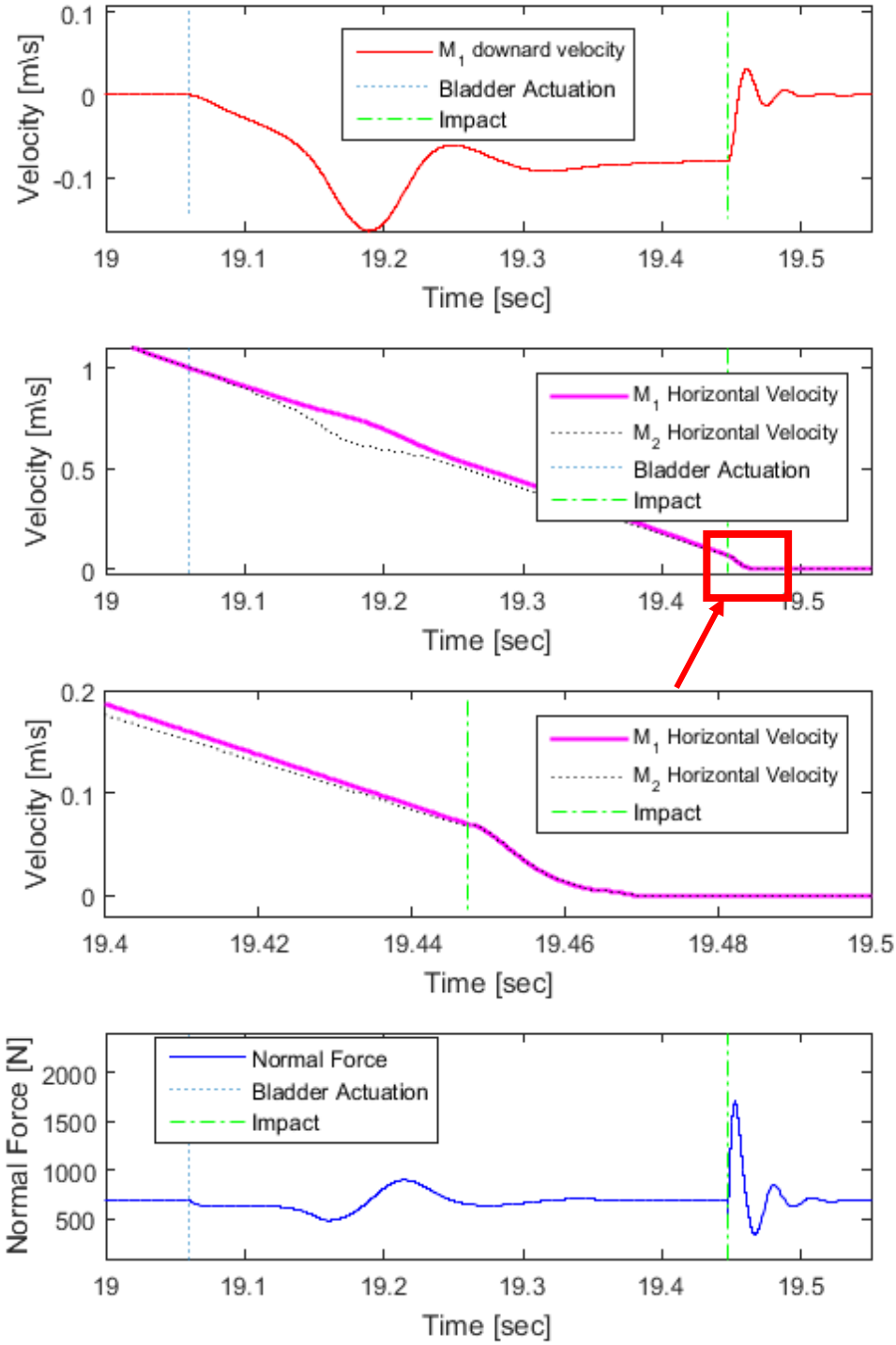

Figure 3.24: Simulation output of bladder actuation at 1 m/s of horizontal slip. Figure depicts downward velocity of M_1, horizontal velocities of both masses, a zoomed in figure of the period during impact of the masses, and the normal force generated.

Table 3.3: Stopping times from point of impact of actuated bladders and non-actuated bladders.

Scenario	Stopping Time [sec]
Actuated Bladders	23 ms
Nonactuated Bladders	31 ms

actuation occurs. Note that the stopping time is taken from the moment of impact. The results show a slight gain in stopping ability with actuated vs. nonactuated bladder systems.

The scenarios discussed above highlight many important key factors that potentially govern the proposed orthotic device's ability to mitigate slip. Note that in order to demonstrate the key behaviors of the system, the bladders were actuated at $v = 1\ m/s$, which is greater than the critical slip velocity of 0.5 m/s discussed in Chapter 2.

Had the bladders been actuated at speeds less than $v = 1\ m/s$, the system would not have experienced impact before forces of friction stopped the horizontal motion. This is because the deflation time of the bladders is greater than the time needed for friction between the shoe and ground to stop the system. It is more reasonable to actuate the bladder system at speeds less than 0.5 m/s as this best optimizes the ability of the orthotic device to mitigate slip. In a more realistic scenario, a person experiencing forward slip will most likely increase in forward velocity over time rather than decrease. However, the simulation scenario does provide insight into determining if the bladder system can deflate fast enough before the user reaches speeds in excess of 0.5 m/s. Cham and Redfern found that, in the case of a person who experienced a slip that resulted in a fall, the user's foot often reached speeds greater than 0.5 m/s in less than 200 ms [5]. Therefore, bladder systems that require 400 ms of deflation time may not be able to generate impact soon enough to produce significant slip-mitigating effects.

This finding indicates that fall time, or the time it takes for M_1 to impact M_2, is a key limitation to the device's performance. The variable fall time is affected by the bladder wall stiffness, the height of the bladder, and the rate at which air flows out of the bladders. During empirical testing performed in Chapter 4, it is shown that the rate of air flow out of the bladders plays the largest role in this process given the relatively small stiffness of the bladder walls.

The ability to generate large normal forces that can mitigate slip, and the potential to create stiction using directional compliancy, provided justification that a device with the ability to mitigate slip may be feasible. The next chapter outlines the construction of a bladder prototype and subsequent testing of the various models. Using the results from empirical testing, a new model focusing on impulse is generated at the conclusion of the testing. The model highlights the ability of the device to potentially mitigate or reduce slip for a variety of bladder heights.

Future modeling efforts should focus on the optimization to minimize fall time while still maintaining significant impulse from impact. However, the Simulink model used to make these initial findings first needed to be validated for accuracy via empirical testing. This process is discussed in Chapter 4.

The simulation is the culmination of several individual models discussed throughout this chapter. The simulation results depicted in this thesis do not represent an optimal design, but rather were selected based upon flow rates (valve systems), materials, and COFs that were assumed prior to empirical testing. Although this thesis presents the research in a sequential timeline that first describes modeling techniques followed by empirical testing, it should be noted that some overlap did occur over the course of the project. Empirical testing was often used to troubleshoot and refine the models presented above and simulations were often used

to understand empirical test results. However, the majority of research was conducted in the timeline presented in this thesis.

4. BLADDER MODEL VERIFICATION

This chapter outlines the construction of a prototype bladder and subsequent testing to validate the accuracy of the models in the previous chapter. The construction process is outlined and simplified testing procedures for each model are discussed. The Ankle Foot Simulator [36] (AFS) is used to perform the tests. The models discussed above are then altered according to empirical testing results and utilized to better evaluate slip mitigation.

Bladder Prototype Construction

With maximum impulse as the target focus of the study, it was desirous to test a simple prototype concept of what the bladders of the proposed shoe structure would look like in conjunction with the simulated models to more accurately approximate the orthotic device in use. A prototype would also allow validation of the models discussed in the previous chapter. In an effort to maximize impulse, the prototype would need to deflate quickly to generate significant impact forces but also be sturdy enough in structure to support a human. The prototype was therefore constructed using a process created by Wang who created shoe bladders similar to the ones described in this thesis [2] [3]. The prototype bladders were first modeled using SolidWorks software and constructed in a hard-plastic form using 3D printing. The plastic was then used to mold a negative of the bladder structure out of *Mold Max* rubber that was then used to mold the desired rubberized model. The bladders were adhesively attached to one of Wang's mechatronic soles that incorporate a wireless valve actuation system.

Figure 4.1 depicts the CAD model and Figure 4.2 depicts the rubberized model attached to the mechatronic sole.

AFS and Natural Frequency Testing

To perform validation testing, an apparatus termed the Ankle Foot Simulator (AFS) was utilized to perform many of the testing procedures in this thesis [36]. However, these tests would most likely induce several large forces and oscillations on the structure of the AFS that could interfere with data collection from sensors. It was therefore necessary to conduct a

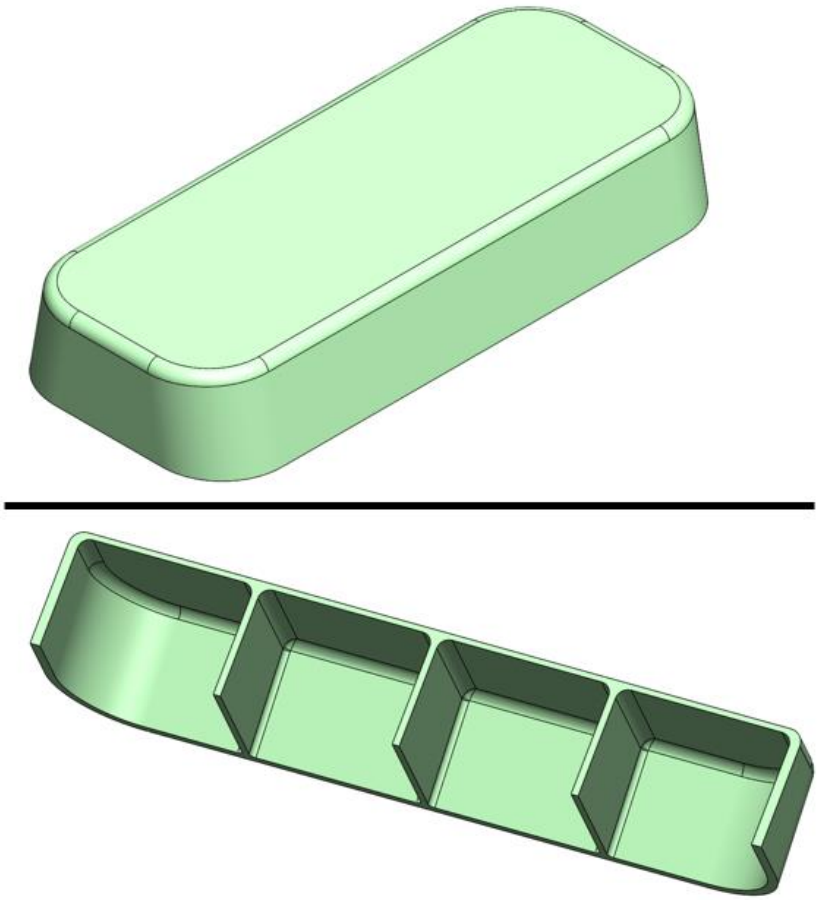

Figure 4.1: CAD model of bladder prototype. Top picture shows full prototype looking down. Bottom pictures shows cross section of prototype looking up.

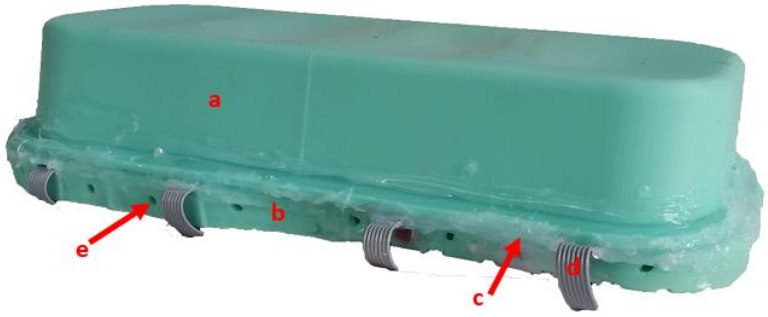

Figure 4.2: Bladder prototype mounted to mechatronic shoe sole. a) Bladder system. b) Mechatronic sole with valve actuation system. c) Silicone glue used to bind bladders to sole. d) Ribbon cable used for communication and power to valve system. e) Valve port holes for deflation, 16 in total.

natural frequency test on the AFS in order to distinguish oscillations from testing procedures and oscillations from structural compliance. This was performed by exciting the AFS force plate with an impact from a rubber mallet while recording the force plate normal force readings. Figure 4.3 depicts the graphical results of the test.

The test was also repeated using an accelerometer attached to areas along the AFS where the greatest impacts would hypothetically occur. However, the results of this test proved difficult to determine low frequencies and were therefore not utilized.

The results of the AFS natural frequency test via the force plate displayed a natural frequency of roughly 20 Hz. As will be discussed later in the thesis, the frequencies recorded during empirical testing of the bladder prototype system were around 6 Hz. These results gave reasonable justification to assume that natural frequencies of the AFS would not interfere significantly with testing procedures.

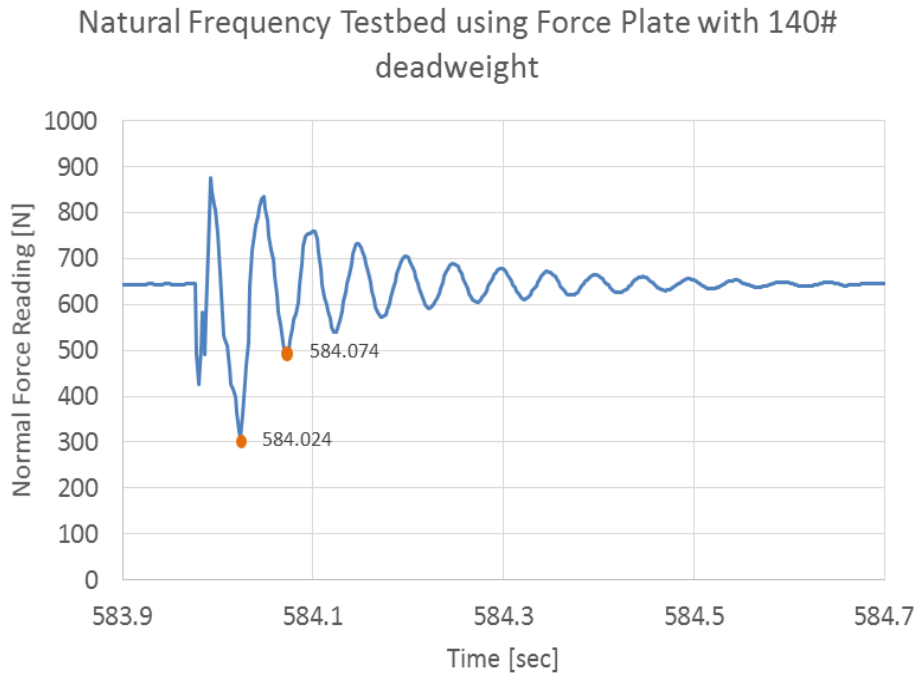

Figure 4.3: Force plate reading results of AFS natural frequency test. Indicated data points are used to approximate vibration period.

Bladder Beam Model Validation

In order to validate the structural beam model of the simulation, a second bladder prototype was constructed without adding the mechatronic shoe sole. The walls of the bladder system were punctured with holes large enough to allow for very low resistance fluid flow, thereby mitigating force readings due to compressed air. Using a vertical saw-tooth profile, the AFS, with an attached rubber foot mold, was programmed to perform a simple reciprocal motion on the bladders in order to generate a force vs. displacement curve. From the data and using equation (4.1) where *K* is the spring constant, *F* is the reaction force, and *x* is the displacement, a good linear approximation can be made to derive a *K* value of 2000 N/m. Using equation (3.7), a damping force was also derived for the bladder system.

$$K = \frac{F}{x} \tag{4.1}$$

Figure 4.4 depicts the results and resultant linear equation fit. The results were then compared to the axial post-buckled model spring constant to determine slope similarity. The results depict the profile generated by force vs. displacement for the prototype as well as an equation of fit for the linear region of the data. For reference, the post-buckled stiffness model is plotted alongside the data with corresponding linear force vs. displacement equation. The empirical testing shows a highly linear profile ($R^2 = 0.995$) in the 5 mm to 30 mm range during bladder compression. The figure shows some discrepancy between the empirical results and calculated spring constant. Initial compression from 0 mm to 5mm demonstrates an abrupt increase in force, which is attributed to initial deflection and buckling of the beams. Above 30 mm deflection, the walls are nearly fully collapsed and begin to sandwich and create a solid mass of rubber. None of these effects are captured by the post-buckled beam model. Likewise, within the linear region from 5 to 30 mm deflection, the post-buckled model has roughly 37%

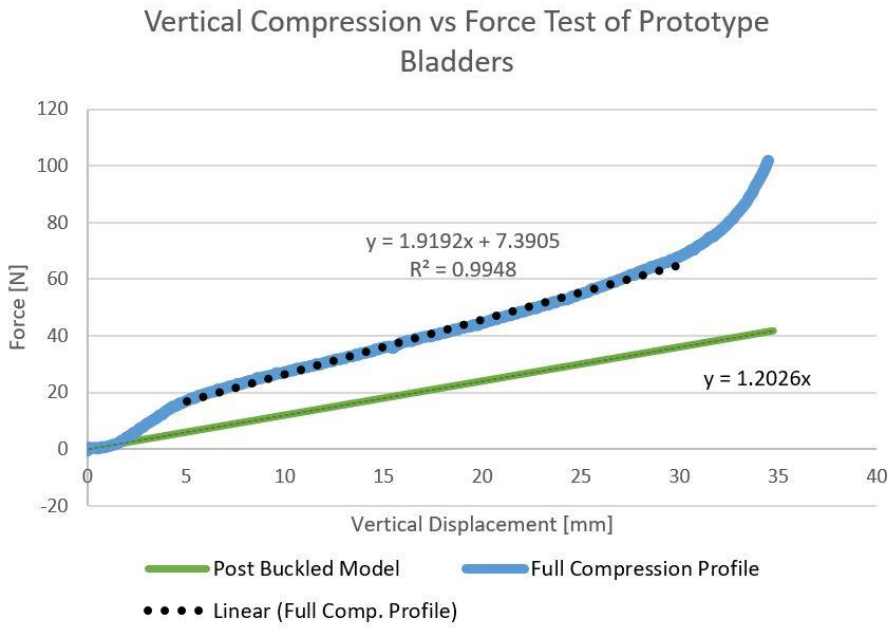

Figure 4.4: Results of force vs. displacement compression test of bladder system. A trendline for the linear portion of the compression testing data is added as well as the equation of fit. The slope of the post-buckled stiffness model is shown for reference.

less stiffness than the empirical testing. This discrepancy is not surprising since the outer wall forces were neglected during simulation and only inner walls separating bladders were accounted for. The test does highlight the effects that the outer walls have on the system stiffness and that more complex models will be needed in the future for more accurate modeling techniques. However, the results do give reason to believe that, if the effects of the outer walls were included in the model, the post-buckled model of the bladder walls may merit some validity. Other modeling techniques, such as FEA, could be more appropriate in future work to potentially more accurately determine a projected response curve of the bladder system.

Air Model Validation

A high rate of air flow in the system constitutes a greater impulse due to increased impact velocity of the user's foot. To test the air flow models of the bladder system, a person stood atop the bladder prototype on the force plate of the AFS while the valve system was actuated. The AFS recorded the normal force experienced by the force plate and the motion of the person was captured with a 60 FPS camera. Figure 4.5 shows the normal force readings of the test aligned with screenshots of the video footage. The figure demonstrates that the changes in normal force were due to oscillations in air flow through the valves and not due to impact. The actual impact of the person and the shoe sole exhibited negligible change in normal force. Note that the subject performing this test represented about 140 lbs of force. The air took roughly 600 ms to deflate from the bladder system, or 33% longer than the simulation prediction. This is most likely due to other flow resistance areas within the valve system that were not accounted for. This may imply that losses from the orifices are significant because resistance due to bladder structure is shown later in this chapter to be negligible. Therefore, the

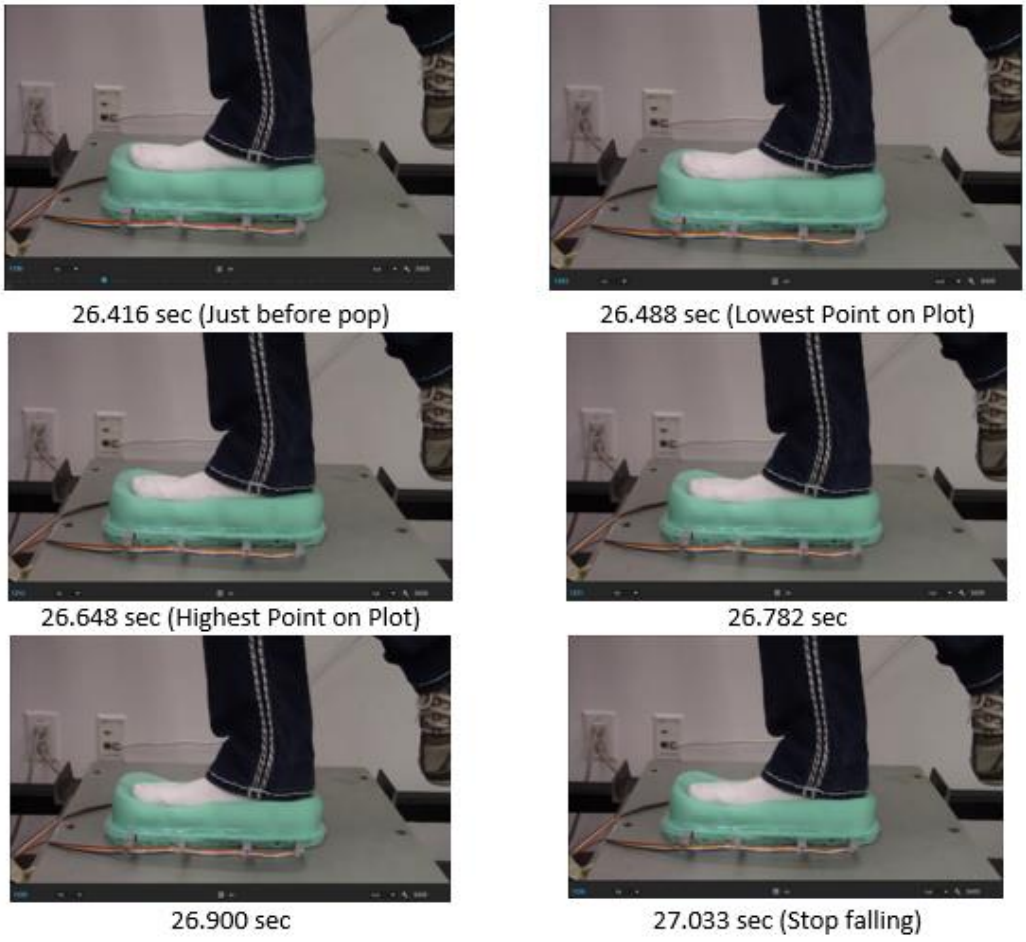

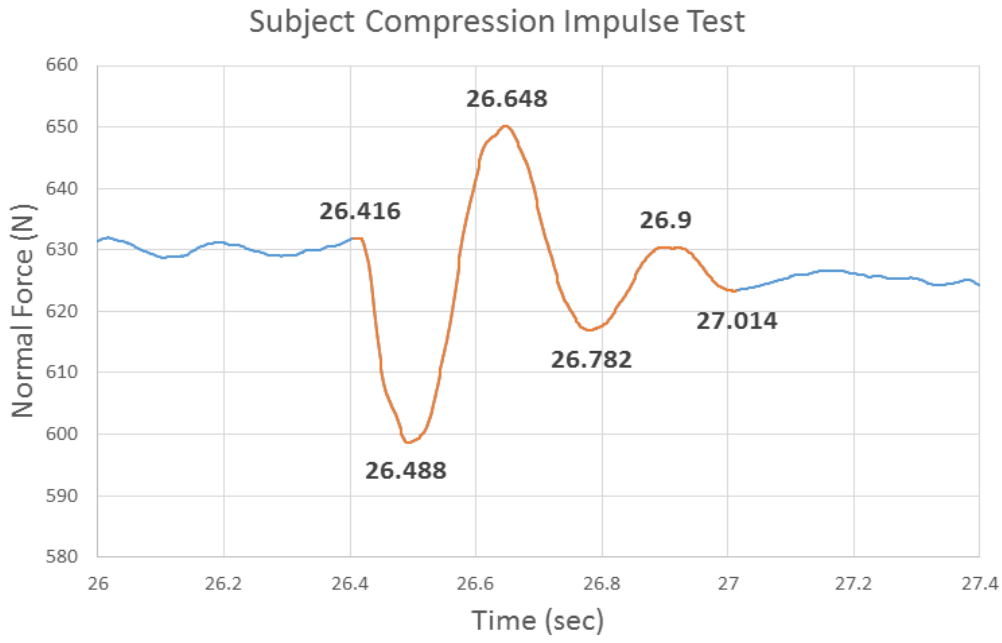

Figure 4.5: Normal force readings aligned with screen snapshots of the bladder deflation show the valves unable to produce the required air flow needed for significant change in impact forces.

majority of the flow resistance comes from the valve system. Future work would most likely require empirical testing of each component within the air flow mechanisms. The models generated from such testing would identify components causing the unaccounted flow resistance, and allow for more accurate air flow predictions.

Because the bladder system could not actuate fast enough to generate meaningful impact forces, it was decided to use the prototype discussed in the previous section that was used to validate the beam model. This prototype exhibits very little air flow resistance and would allow for ideal testing of friction force manipulation resulting from impact forces. As low flow resistance is desirable to generate impact forces, using this prototype in future testing would allow for some validation of the contact models and to determine if such a system could be used to mitigate slip in a theoretical setting.

Impulse Testing Using AFS

The next step in the procedure was to verify the contact models from equations (2.4) and (2.5) that are used in the slip reduction formula of (1.5). It was also desirable to understand how the coefficient of friction, μ, changes with impact. A test set-up was designed to replicate a shoe system with bladders sliding on a surface while undergoing impact and is depicted in Figure 4.6. The test is constructed as follows:

1. A melamine-coated board was rigidly attached to the force plate of the AFS. Melamine was chosen for its rigidity and low friction surface.
2. Wooden dowels, 2” diameter, are placed between the melamine board and a rigid aluminum plate. The dowels are lightweight and therefore provide little rotational or linear inertia.

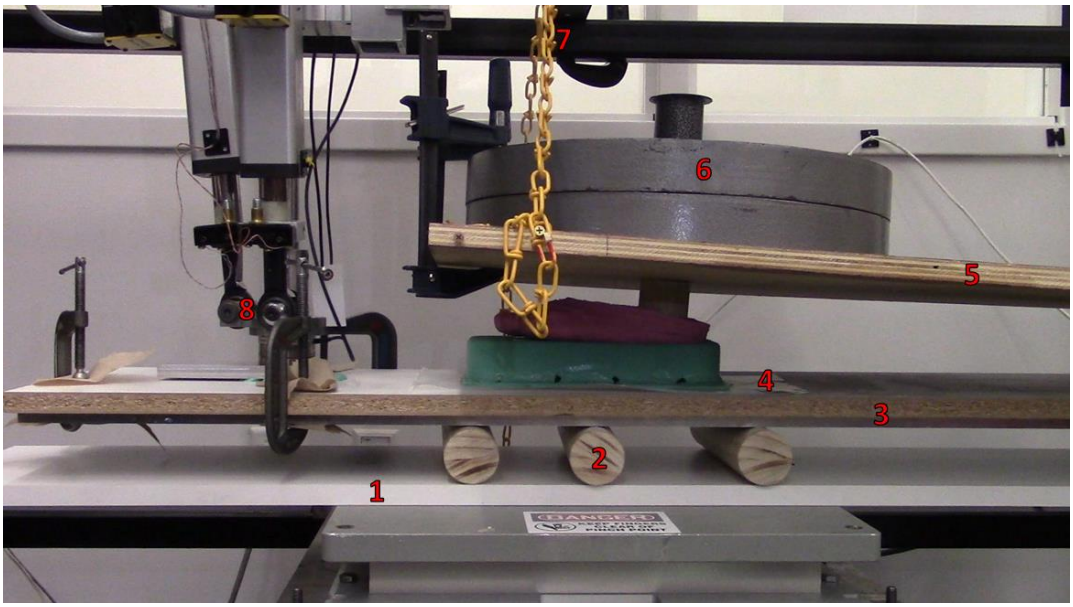

Figure 4.6: Impulse test set-up.

3. A second melamine board was clamped on top of the aluminum plate. The plate was used to increase rigidity as this board/plate combination replicates the very stiff ground. The board was coated in a layer of dry PTFE lubrication to provide an extra slippery surface. Note that previous test attempts had used a liquid mixture of glycerin and water. However, it was discovered that the rubber bladder acted like a squeegee on the liquid lubricant making slip difficult to achieve. Therefore, the dry lubricant was used for purposes of understanding system dynamics and validating the models of Chapter 3.
4. A layer of 4 mil plastic sheeting was laid on top of the board with the bladder shoe system placed atop the sheeting. The silicone material of the bladder shoe system created a sticky bond with the plastic sheeting that allowed for negligible movement between the two surfaces.

5. A large sheet of plywood was suspended above the bladders and rotated on a hinge rigidly mounted to the side frame of the AFS. A silicone-molded human foot was rigidly attached to the bottom of the plywood to better approximate the contact area and compliancy of a human foot.
6. Large weights, approximately 100 lbs, were placed on top of the plywood. While this weight would ideally replicate the weight of an average person, a smaller amount was used due to load limitations of the AFS force plate and load cell.
7. The plywood was suspended by a chain that was linked to a drive screw mounted to the frame of the AFS. The chain was released by turning the drive screw that dropped the weights onto the bladder system. Note that small angle theorem was assumed for the hinged plywood.
8. The gantry of the AFS, which included a load cell, was rigidly attached to the top melamine board and was programmed with a horizontal saw-tooth profile to move forward and backward at a constant velocity.

The variables of interest in this test were the normal force felt by the force plate and the coefficient of friction created by the horizontal force, felt by the load cell, during impact scenarios and nonimpact scenarios. The coefficient was calculated by rearranging equation (1.1) into equation (4.2).

$$\mu = \frac{F_N sign(v_x)}{F_f} \tag{4.2}$$

F_N is the normal force felt by the force plate and F_f is the horizontal force experienced by the load cell. The results of the test, depicted in Figure 4.7, initially displayed odd behavior when normal force was plotted alongside COF. The results show large spikes in normal force as expected. Upon closer inspection, a response frequency of 6 Hz is noted, which is well below the 20 Hz natural frequency noted earlier. However, the horizontal force is out of phase with the

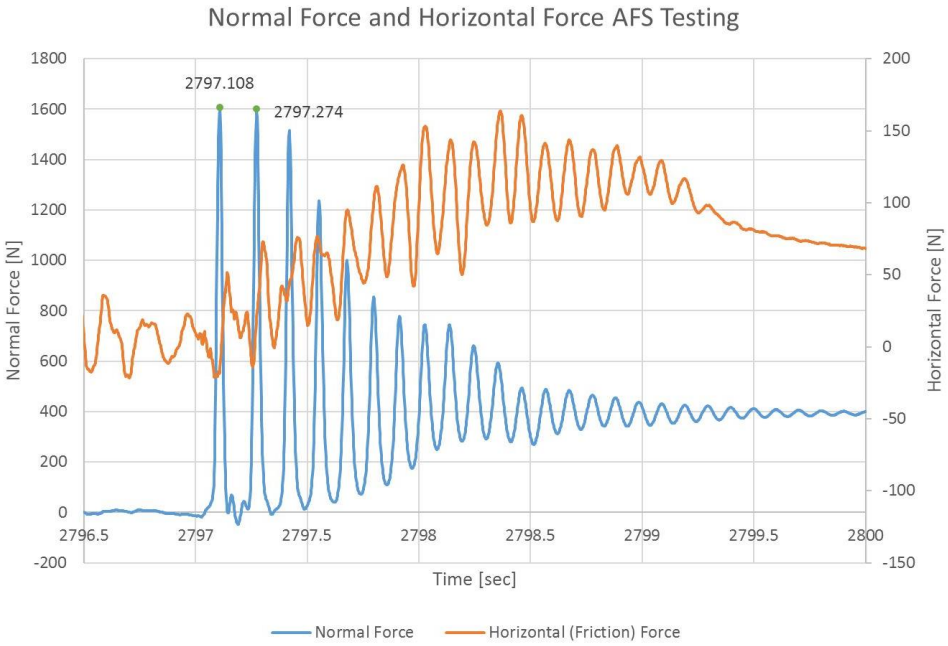

Figure 4.7: Results of first AFS test. Normal force, recorded by force plate, plotted alongside horizontal force, recorded by load cell. Response frequency was also calculated from the data.

normal force by roughly 40 ms, which is contrary to the physics of equation (1.1) that state friction force should increase proportionally with increased normal force. The calculated COF was therefore unreliable because equation (4.2) would often lead to a divide by near-zero scenario. Possible explanations for this unexpected behavior in horizontal force and normal force will be analyzed in the next sections.

In order to verify that normal force results were not significantly impacted by the moving components of the test, a similar normal force experiment was conducted in a simpler set-up where the load was dropped onto the bladders at rest on the force plate. Figure 4.8 shows the test set-up and Figure 4.9 depicts the results. The results are similar to that of Figure 4.7 and therefore can be used to validate the contact models.

The test set-up in Figure 4.8 was also used to calculate deflation time for the bladder systems. Using video feedback, the time from the release of the weight to contact with the force plate is roughly 100 ms. Using the calculations of equation (3.21) in Chapter 3, the time for a

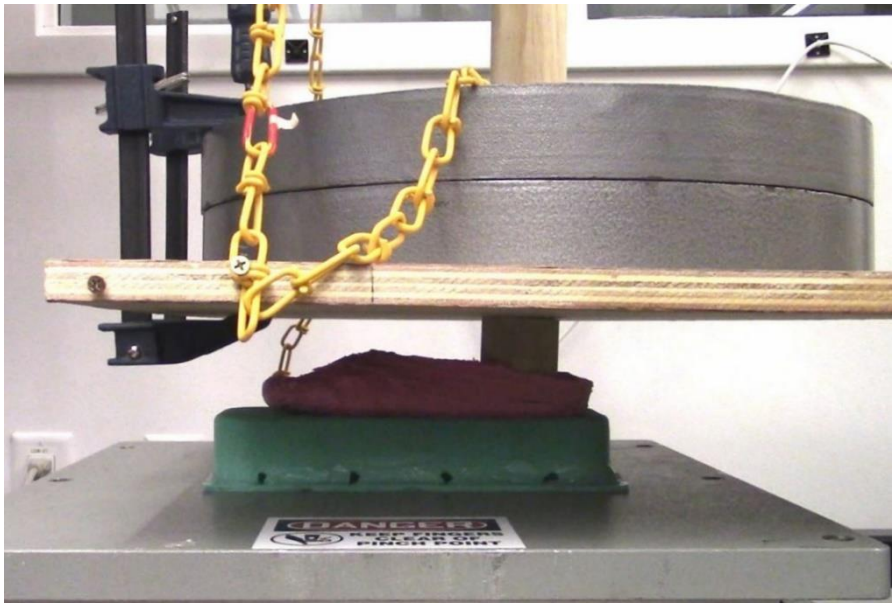

Figure 4.8: Test set-up for simplified normal force readings using AFS.

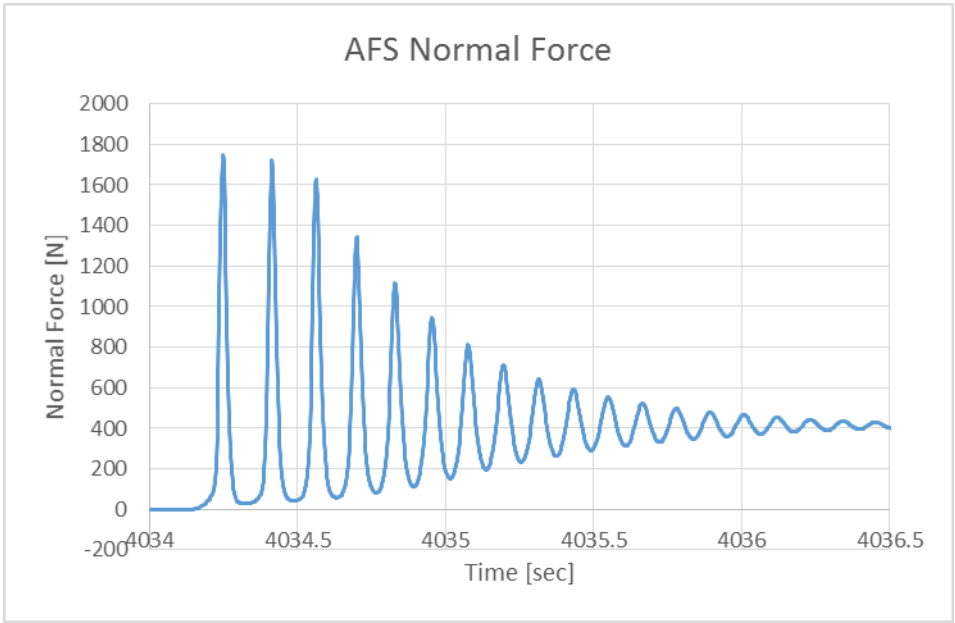

Figure 4.9: Results of simplified normal force readings using AFS.

mass to free fall from this height was about 90 ms. This indicates that the bladder walls contribute a negligible amount of resistance to air flow and that the majority of the flow resistance observed in the previous section is most likely an attribute of the valve system.

Using the results from Figure 4.9, a contact model that incorporated the contact equations, (2.4) and (2.5) or the Flores and Gonthier equations, as well as the spring and damping parameters of the bladder system can be created in order to predict contact response. The spring force utilized in this model is the empirically derived equation from Figure 4.4 and the damping was determined using equation (3.7). Using Simulink, a dynamic model that simulated a mass dropped from a height roughly equal to that experimentally used in Figure 4.8 was developed. Note the model is simplified to only simulate the vertical motion dynamics. In the simulation, the mass collides with a spring and damper from the bladder system and generates contact forces using equations (2.4) and (2.5). Figure 4.10 depicts a schematic of the

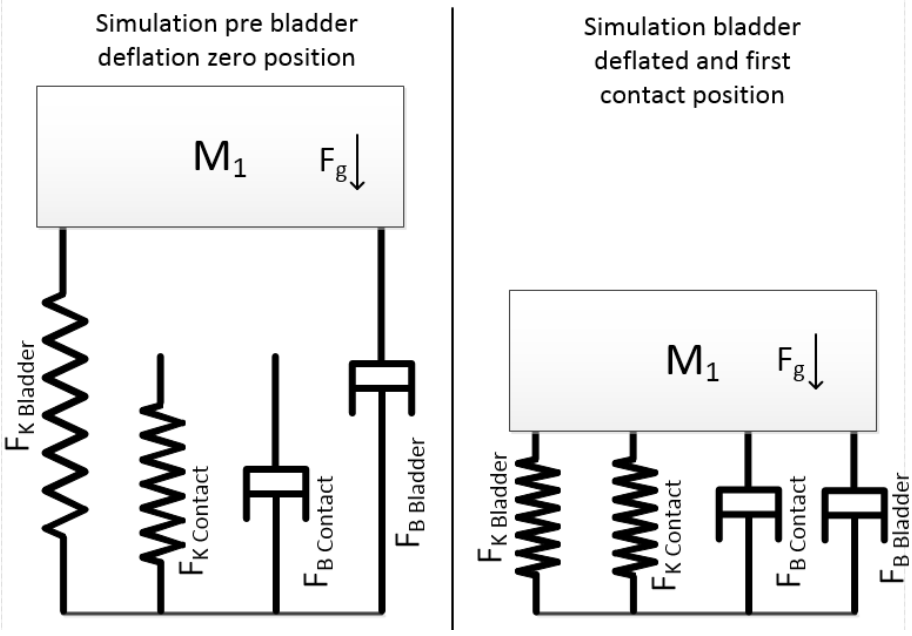

Figure 4.10: Graphical depiction of contact simulation.

Simulink model set-up. Precautions in the simulation set-up were taken so that the bladder and contact forces could never exert a downward force on M_1. Figure 4.11 depicts the force profile action on M_1 during the simulation. It should be noted that for these simulations, an arbitrary expected damping coefficient of 0.9 is used.

Figure 4.11 shows that both the Flores and Gonthier contact models can accurately mimic the amplitude of the response of Figure 4.9. The results also correspond well to the free fall time of the mass before it contacted the force plate, about 100 ms, which was deduced from video analysis of the prior experiments. Other data characteristics, such as settling time and period, are specific to the test set-up and will need to be altered in future models to mimic experimental results using human subjects. These characteristics are difficult to predict for a user without experimental study due to the complexity of the human physiology. This

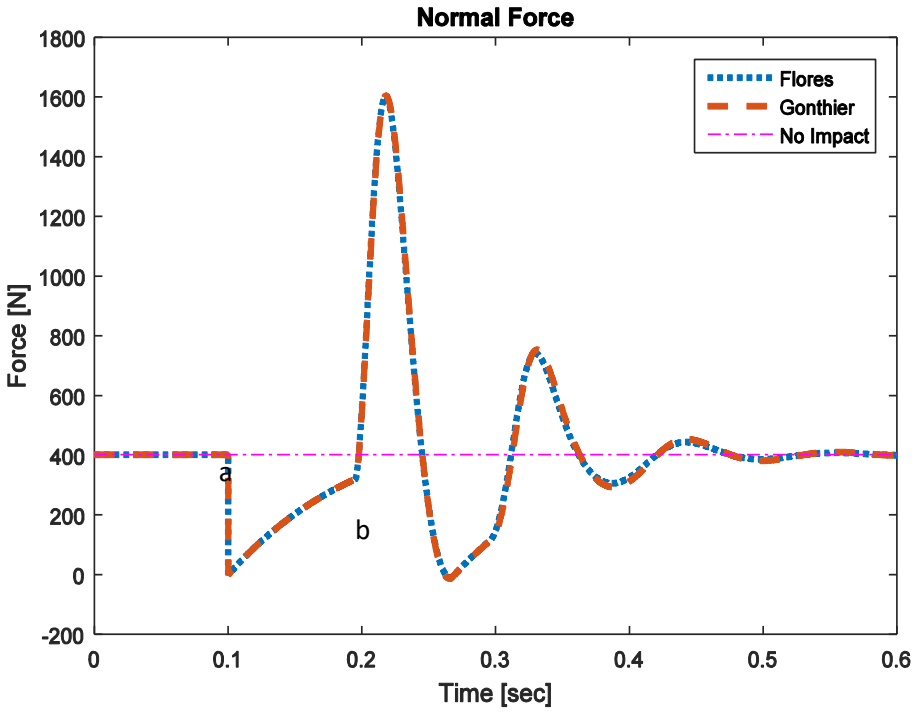

Figure 4.11: Simulation of contact model results. Point “a” is where the fall begins. Point “b” is the impact of the mass with ground.

incorporates many joints, muscles, and possible cognitive factors that will affect the normal force and friction force response. To determine the effects of these factors, a large study involving human subjects as well as a bladder system that can detect slip and actuate a high flow rate valve system will need to be developed. As previously mentioned, this future work is outside the scope of this thesis.

AFS Signal Delay Analysis

The discrepancies in normal force shown in Figure 4.7 gave reason for a careful examination of the test set-up of Figure 4.6 and subsequent video footage. Playback revealed that, although the melamine board clamped to the aluminum plate provided a solid surface to replicate the ground, the impact forces of the weights still produced bending moments and undesired vertical movement of the board/plate structure. This movement was amplified at the ends of the board/plate where the gantry and load cell were attached and most likely induced moment forces that could interfere or invalidate results. Another possible reason for the abnormal behavior could be due to observed signal delay between the load cell and force plate. These and other discrepancies, such as the imperfections in the wooden dowels, questioned the validity of the horizontal force results and gave reason for further test improvements. These improvements will be discussed in the next section.

To determine if a signal delay between force plate and load cell was causing discrepancies, a simple test was designed that mimicked the action of a large normal force creating a horizontal force. The AFS was retrofitted with a rigid aluminum plate attached to the load cell and was programmed with the same saw-tooth profile while applying just enough force to roll a wooden dowel back and forth across the force plate. During the horizontal movement, the aluminum plate was hit vertically with a rubber mallet, thereby driving a normal force spike

into the force plate and subsequent horizontal force spike in the load cell. The simplicity of the test removed many possible mechanical issues that could lead to signal delay. The results are depicted in Figure 4.12 and demonstrate a roughly 6 ms delay between signals in addition to the aforementioned 40 ms delay. The cause of this 6 ms delay is most likely due to a signal filtering process within the AFS code. Subsequent investigations found that filtering mechanisms exist inside the AFS Simulink model that could reasonably be assumed to be the root cause. Figure 4.13 shows the test set-up.

This 6 ms delay combined with observed moments and other instabilities gave reason to pursue another test set-up. Because previous testing validated contact models, a new test set-up could be simpler now that both impact forces and horizontal forces need not be tested together. This simplified horizontal test is discussed in the next section.

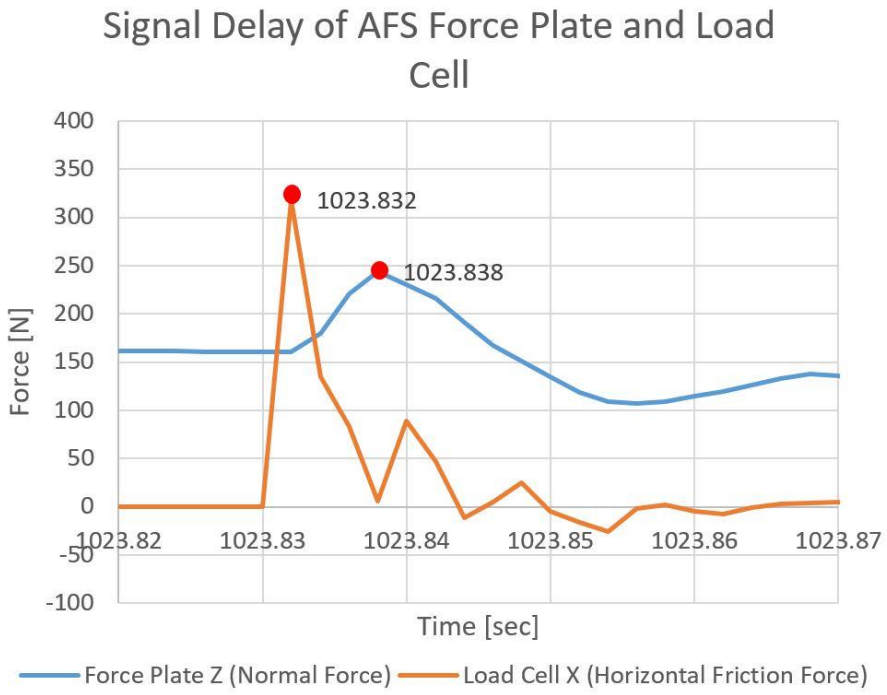

Figure 4.12: Results of signal delay test. Note roughly 6ms between peaks of force spikes.

Figure 4.13: Signal delay test set-up.

Simplified Horizontal Force Test

Since the normal force response of the system was determined in the test of Figure 4.8, the AFS itself can be used to replicate the impact forces of the weights. Such a set-up has the potential to more accurately determine horizontal force response without the use of a complex testing apparatus and highly rigid materials to act as ground. A simplified test was devised with a goal to replicate the normal force spike amplitudes observed in Figure 4.9, allowing better understanding of how the impulse affects horizontal forces and COF. The test set-up is illustrated in Figure 4.14.

The AFS was outfitted with 1) a single melamine board attached at the force plate and 2) a layer of PTFE dry lube-coated plastic sheeting to provide a slippery surface. A layer of 3) thin silicone was added to provide stiction between the gantry and plastic sheeting. It also protected the components from gouging and worked to distribute forces. The load cell was outfitted with 4) a rigid aluminum plate. The AFS was programmed to apply a constant force on the force plate

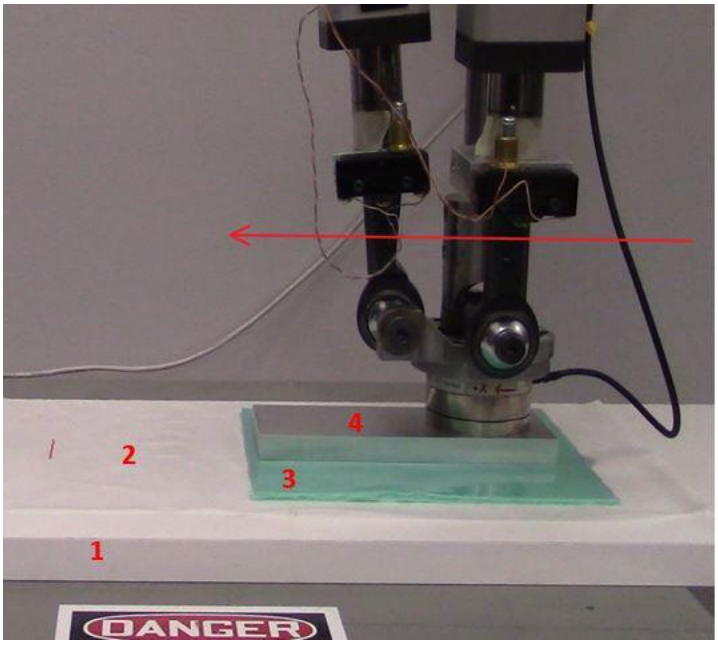

Figure 4.14: Simplified AFS test to determine horizontal force reaction. 1) Melamine board rigidly attached to force plate. 2) PTFE coated sheeting. 3) Silicone rubber sheet. 4) Rigid aluminum plate.

roughly equal to 90 lbs or the weight shown in Figure 4.8, with the gantry moving at a steady state horizontal velocity. While applying this force, the gantry moved in a constant horizontal velocity via a saw-tooth program. During the program, the gantry exerted an immediate downward force on the force plate that caused an immediate spike in horizontal force. This created a simplified scenario where the relationship between normal force and horizontal force during impact could be explored. The results proved to be more in-line with equation (1.1) with horizontal forces increasing along with normal forces. Figure 4.15 depicts the results by plotting horizontal force alongside normal force as well as COF alongside normal force. Note that the data in Figure 4.15 were skewed to reflect the 6 ms delay in signals. Region “a”, as specified in Figure 4.15, displays the constant normal force exerted by the AFS during the test and point “b” specifies the region when the immediate downward force is applied.

The results show that spikes in normal forces lead to increased friction coefficients and therefore greater stopping or slip mitigating ability. These findings are exciting as they show that COF can be momentarily manipulated to increase friction forces. These increased friction forces could be used in conjunction with equation (1.5) to significantly reduce the slip velocity or, if the impulse is large enough, mitigate the slip completely by moving the user from the kinetic COF region to the static COF. Future testing on common slip surfaces that analyze the amount of impulse needed to generate this increased COF will need to be performed in order to gain a better understanding of this phenomena.

Note at point “c” in Figure 4.15 that there is a slight dip in the normal force profile that corresponds to a dip in horizontal force. This dip in normal force is likely related to oscillations in the AFS as it tries to maintain a load. It is interesting to note how much the COF changes during this portion of the plot and suggests that even small changes in normal force can have large impacts on the COF. It is also interesting to see that after point “b”, the horizontal force increases with duration of high normal force loads. This phenomenon is believed to mostly be attributed to the thin rubber layer that is placed within the test set-up. During consecutive testing, it was noted that the phenomena seen after point “b” increased with increasing thickness of the silicon rubber. It was therefore assumed that the increase in horizontal force was due to shearing within the silicon rubber and that thicker layers of rubber constituted more shearing. Other shear loads can possibly come from the gantry of the AFS which, while in contact with the force plate, experiences high bending moments.

It is also observed that after the immediate downward force is relieved, a series of oscillating normal and horizontal forces occurs in region “d”. During video playback of the test, oscillations in the horizontal direction of the gantry are observed to correlate with the oscillations of region “d”. These oscillations could represent a slip-stick phenomenon as the

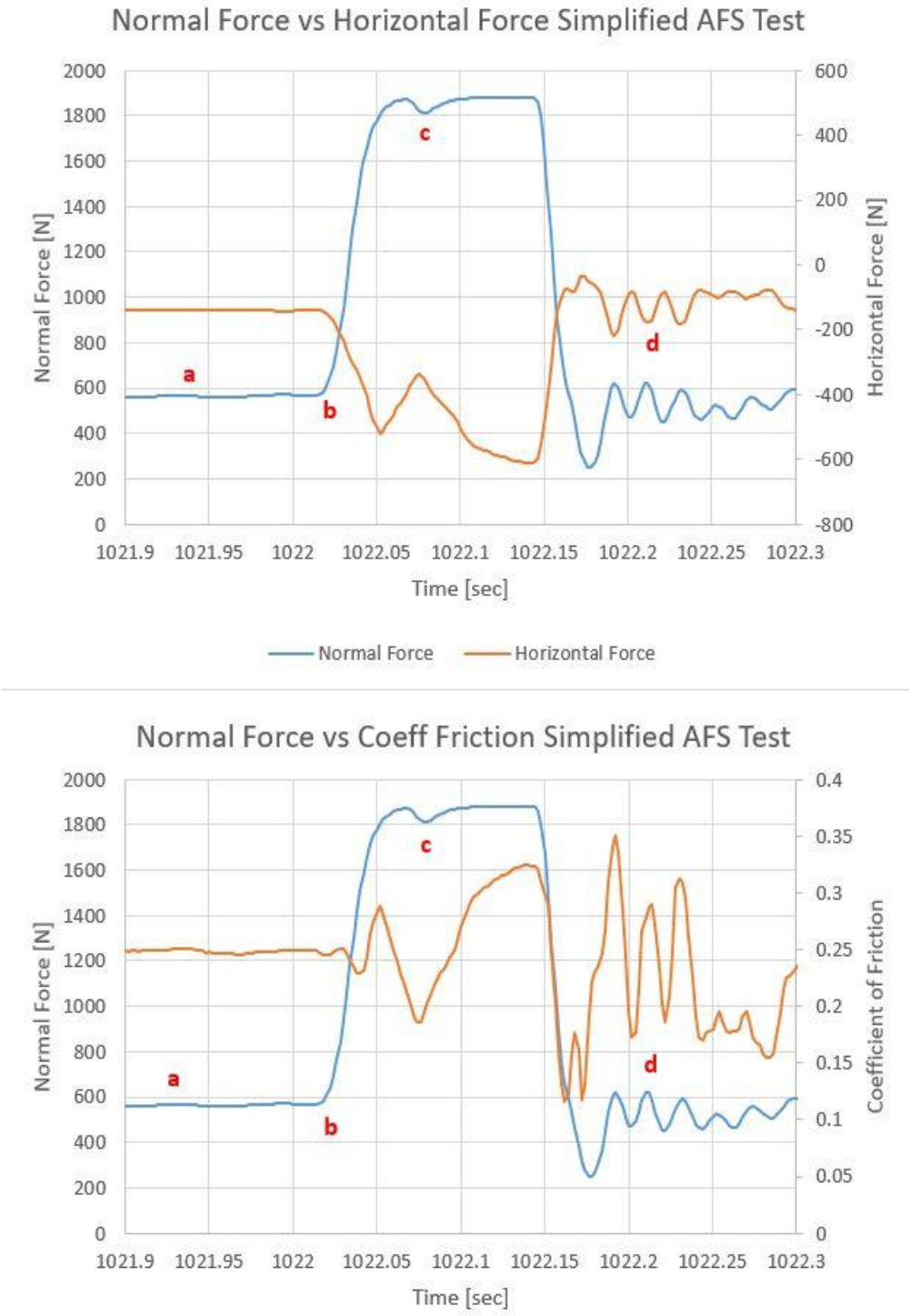

Figure 4.15: Results of simplified horizontal force test. a) The steady state applied force during slip. b) Large impulse is applied. c) Impulse normal and horizontal force response. Also slight dip in normal force most likely due to oscillations in AFS attempting to maintain large load. d) Large impulse force is released and system returns to applied force under slip. Oscillations possibly due to stick-slip phenomena and again AFS attempting to maintain large loads.

gantry attempts to overcome static COF forces. However, it was also noticed that the horizontal velocity of the gantry slows slightly during region “c” due to the increased friction forces and these oscillations may simply be a result of the AFS attempting to correct for the slowed velocity and maintain a desired position. Load maintaining issues, as discussed at point ”c”, may also be present as the AFS attempts to shift from the larger impact force and maintain the 90 lbs vertical force. The AFS horizontal actuators also use long timing belts that will have some compliancy and the frame of the AFS does experience some movement in the horizontal direction when high loads are applied.

A variable often used to determine slipping potential is the Required Coefficient of Friction (RCOF), which is a determination of the minimum amount of friction needed to prevent slip between two surfaces. The data from Figure 4.15 can be manipulated to form a plot of RCOF with bladder actuation vs. RCOF (estimated) without bladder actuation. The data are generated by comparing the steady state friction force from the “a” region in Figure 4.15 and the normal force profile during the test. This plot is shown in Figure 4.16 and demonstrates that RCOF can be reduced during impact.

The results of Figure 4.15 were also used to determine a reasonable kinetic COF between the PTFE plastic sheeting and melamine board. The normal and horizontal forces just before impact were used in conjunction with equation (1.1) to calculate μ = 0.25. This COF is used for modeling purposes in the next section.

Analysis of Impact Model

It has now been demonstrated that generating an impact with the ground can create increased horizontal or friction forces, as well as increased COF. COFs are often empirically derived due to the complexity of the physics governing them and are often specific to the two

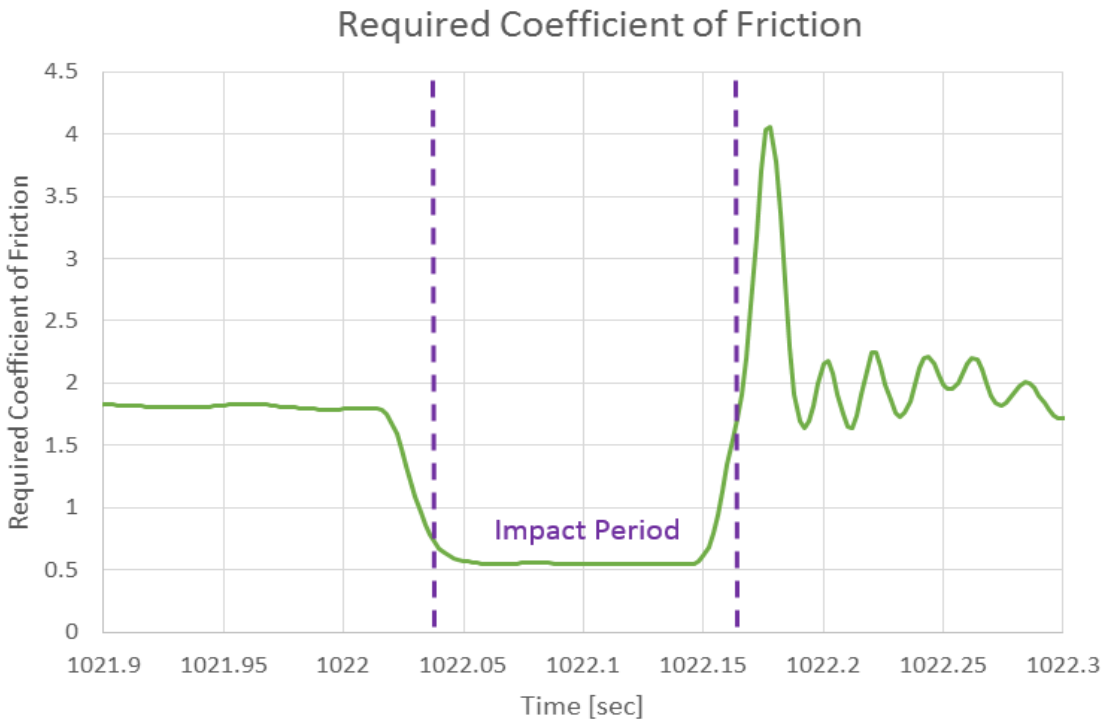

Figure 4.16: Required COF for simplified AFS test.

mating surfaces. Therefore, an analysis of the increase of the COF is best suited to an empirical test and is outside the scope of this thesis. However, assuming a constant COF, equation (1.5) can be used to analyze the impact to determine if a net change in momentum, or velocity can be achieved. Figure 4.11 demonstrates two key areas where friction force is lost and gained that relate to equation (1.5) as highlighted in Figure 4.17. Note that Figure 4.17 utilizes the same Simulink contact model of Figure 4.11.

The first area, shown in red, highlights the mass, M_1, free fall zone where the system immediately sees a drop in normal force that gradually increases due to the compressing bladder structure until impact is reached and contact is made. During this time, friction force is less than what could be achieved had no free fall been experienced because normal forces are lower and therefore constitute a lesser decrease in friction forces. However, once contact is

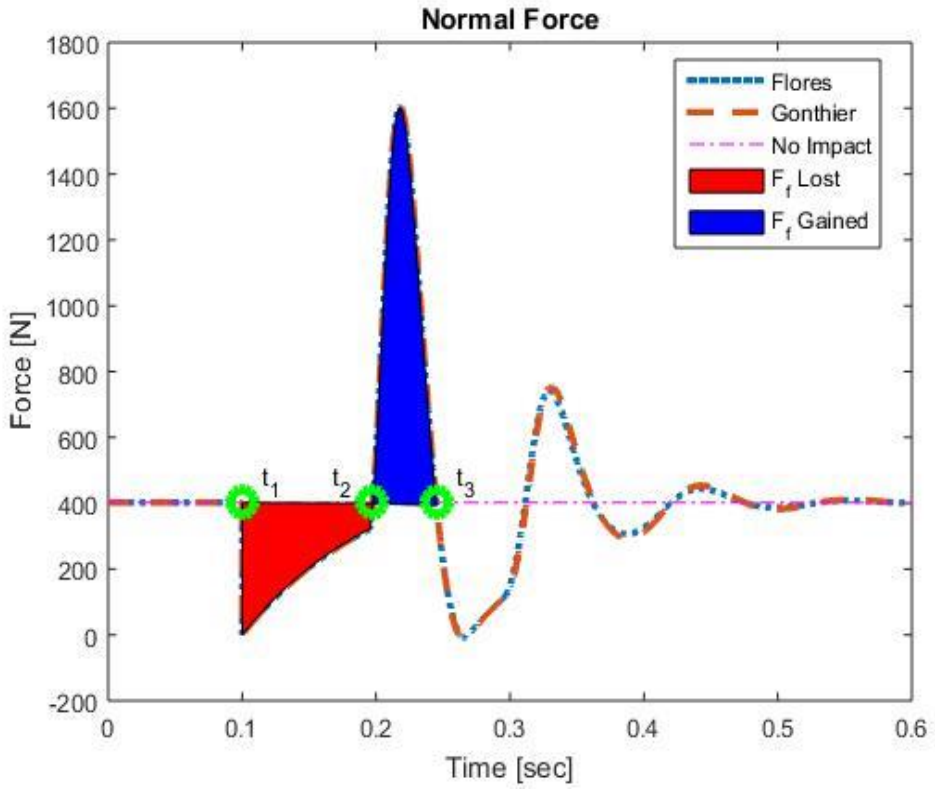

Figure 4.17: Contact simulation results with key areas of friction force gain/loss highlighted.

made, the normal force generated creates a much greater friction force than what the weight of the mass could alone, demonstrated by the second section of Figure 4.17 shown in blue. The first impulse of the normal force response is only taken into consideration, as it is expected that if this first impact cannot achieve any meaningful change in momentum, then subsequent, less powerful strike will not achieve desirable results. Equation (1.5) can therefore be rewritten to reflect these counteracting forces and solve for a net change in momentum, *p*, or by dividing by mass, a net change in velocity, *v*.

$$\int_{t_2}^{t_3} F_f dt \; - \int_{t_1}^{t_2} F_f dt = \Delta v * M_1 = \Delta p \tag{4.3}$$

Using the data from Figure 4.17, equation (4.3) solves to 13.4 kg-m/s or 0.33 m/s if dividing by mass, showing that a net reduction in slip is possible within this scenario. Note that this change represents a minimum value as the COF increases during the contact period, or blue region, of Figure 4.17. Similar simulations with varying mass and bladder heights have been calculated and plotted in Figure 4.18 to further demonstrate the slip mitigating ability of equation (4.3). The figure utilizes a COF of 0.25 as calculated in the previous section.

Figure 4.18 highlights the system performance differences of using varying bladder heights and user weights. At low masses, the net reduction in velocity is similar for the majority of bladder heights shown below. However, as mass increases, the reduction in velocity increases rapidly. This suggests that actuation of such a system should occur when the majority of the user's weight is on the slipping foot so as to maximize slip mitigation effects. Increased bladder

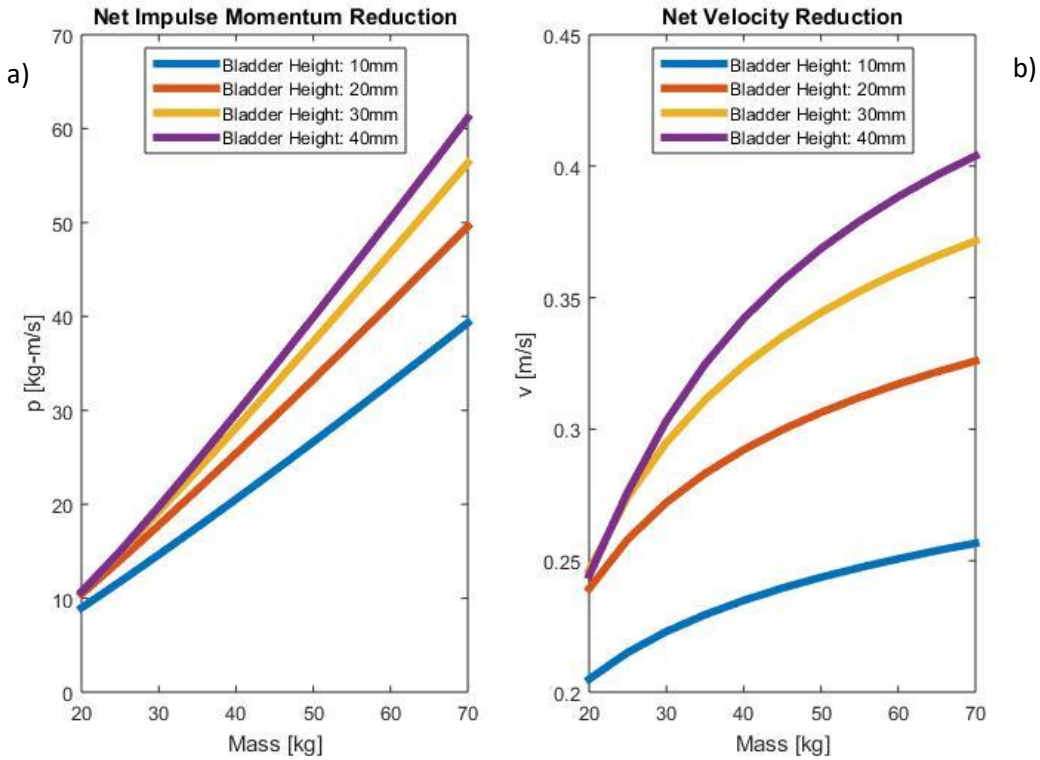

Figure 4.18: Net reduction in a) Impulse and b) Velocity.

heights in general provide significantly greater velocity changes and could possibly be extended to mitigate the critical slip velocity of 0.5 m/s. However, this increase in height can jeopardize the stability of the user during normal gait activity.

With the current system design, mitigating the critical slip velocity of 0.5 m/s will require taller bladder systems. This limitation, however, does not suggest that slip cannot be mitigated or recovered from by using a shorter bladder. The velocity of the user could be reduced to a slow enough speed so as to allow the user more time to recover from the slip before falling can occur. In another case, the system could actuate early on in the slipping process before the critical velocity is reached.

A variation of the test discussed in the previous section was also performed by using the bladder prototype with a shoe sole that does not incorporate the mechatronic valves. The purpose of this test was to acquire the same understanding of impact in relation to horizontal forces and COF while using the bladder system. In this test, the AFS utilized a similar saw-tooth profile but did not apply a continuous load of roughly 90lbs. The same immediate downward force that represents the impact of the user's foot was still utilized; however, the AFS was retrofitted with a rubberized mold of a foot instead of the rigid aluminum plate. Figure 4.19 displays the test set-up.

The test was performed prior to the test discussed in the previous chapter. Figure 4.20 displays the normal and horizontal forces during impact. Video playback of the test showed several phenomena during the procedure that gave reason to the odd behavior exhibited in the normal and horizontal force readings. The results of Figure 4.20 display odd behavior in that horizontal forces appear to decrease with increased normal forces. These results contradict the coulombic friction formula of equation (1.3) and suggest that other system dynamics are significantly impacting the desired behaviors.

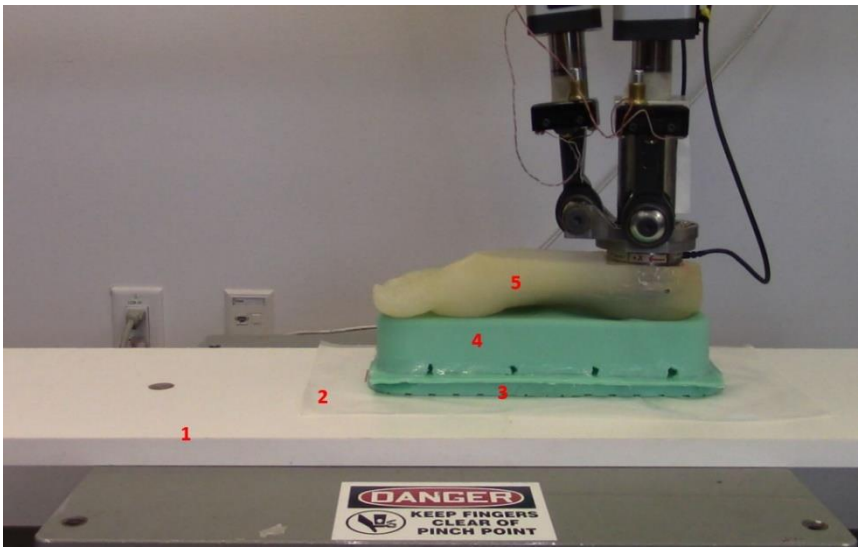

Figure 4.19: Alternative test set-up utilizing bladder system and rubberized shoe sole without mechatronic valve system. 1) Melamine board. 2) Plastic sheeting with PTFE dry lube. 3) Rubberized shoe sole without valve systems. 4) Bladder system with punctured holes for high flow rate. 5) Rubberized foot mounted to AFS load cell.

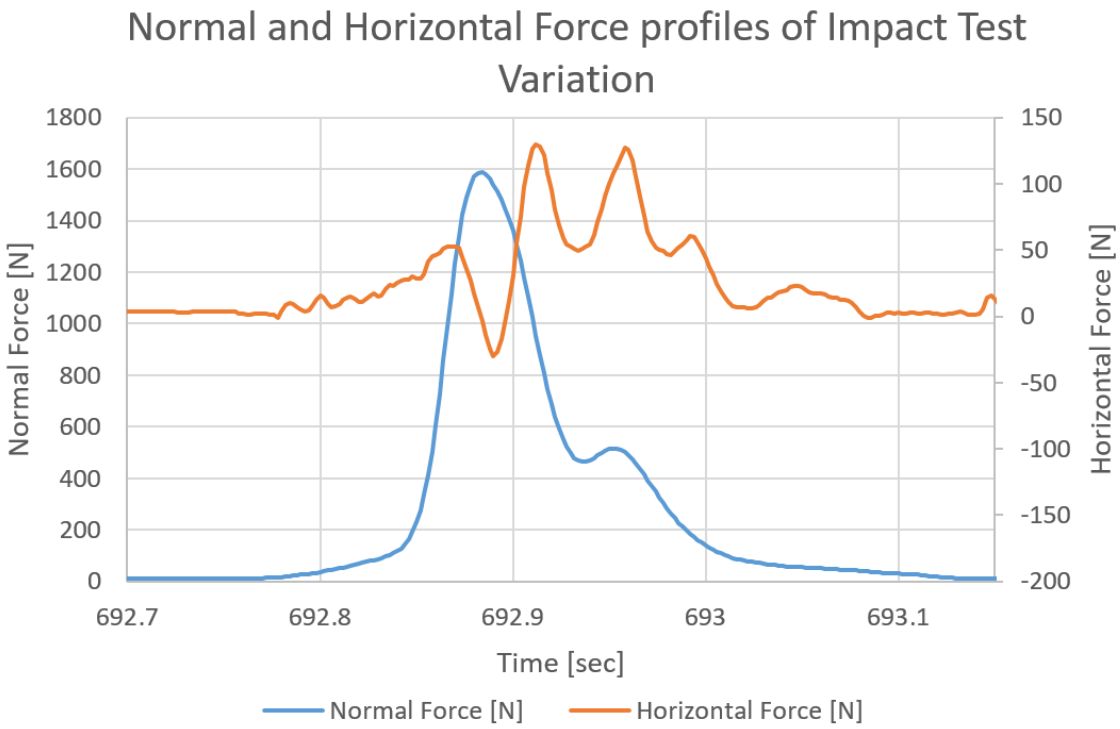

Figure 4.20: Normal and horizontal forces of impact test variation using bladder system and shoe sole without mechatronic valves.

During impact, the rubberized sole is seen to undergo significant deformation that could lead to portions of the surface area between sole and plastic sheet to experience slip phenomena. Another suggestion explores the possibility that, due to lack of a preload force like that of the test discussed in the previous section, the rapid compression of the bladders quickly forces any air out from under the shoe sole or plastic sheeting. This rapid exit of air may constitute an effect where the prototype experiences slip in a manner similar to hydroplaning. The possibility of air underneath the sole could be due to the treads on the bottom of the shoe sole that were not present in most other bladder performance tests.

Given the odd behavior, the tests mentioned in the previous section were performed on grounds that they were better suited to validate the slip mitigating hypotheses of this study. However, this initial test does highlight some of the future challenges of mitigating slip using impact. Future work will most likely include a more in-depth analysis as to the cause of the results displayed in Figure 4.20. Future testing with human subjects may also shed light onto the observed phenomena by providing a more realistic slipping scenario.

5. DISCUSSION AND FUTURE WORK

The hypothesis outlined in this thesis explores the possibilities of using an orthotic device composed of a system of air bladder structures integrated with mechatronic micro-processors and valves that could be used in order to mitigate human slip. While various ideas regarding how the device could achieve this drove the research, this thesis highlights that one promising method of achieving this is to create a large impact collision with the user's foot and the shoe sole or ground. This is established via a standard equation for impulse using the coulombic friction forces as the impulse force. The equation relies heavily on predicting contact forces between two objects in collision and therefore required a multiphysics study of different dynamics using MATLAB Simulink software. Details of the modeling procedure, results, and assumptions are outlined in Chapter 3. Once the models were created to a satisfactory level, a prototype was constructed and prepared for validation testing, which is summarized and discussed in this chapter.

Validation procedures utilized the Ankle Foot Simulator (AFS) to test dynamic forces using a force plate and load cell. Because large impacts were going to be placed on the AFS, it was desirable to know the natural frequency of the parts of the AFS where the impact would occur in order to distinguish between oscillations due to impact and oscillations due to system compliancy. The test was measured using an accelerometer as well as the AFS force plate while being actuated with a rubber mallet. The results of the test in comparison to impact results would show that the natural frequencies of the AFS are significantly higher than those of the

impact testing and should pose minimal error.

The bladder beam model was tested via a simple empirical test using the AFS to apply displacement in a vertical saw-tooth motion. Vertical forces were recorded to generate a force vs. displacement curve for the prototype. The underlying assumption of this model was that the outer wall structure would not significantly affect forces when the system was compressed. However, the testing showed that larger forces than expected were experienced during compression and are most likely due to this outer wall structure. Future work could possibly entail a mathematical model that could account for these forces similar to the model developed in this thesis. However, such approaches are difficult because of the complexity of the "T" cross sections of the bladder walls as well as unaccounted curvatures at the bladder structure corners. Ideally, a better model could be developed using more advanced Finite Element Analysis (FEA). However, these types of models often require large computational efforts to achieve the same dynamic time-step responses characteristic of the type of model developed in this thesis.

Air flow through the bladder valves proved to be an obstacle in constructing a device that could generate enough impact force to mitigate slip. Modeling efforts utilized a simple piston-cylinder model with calculated flow resistance using manufacturer-supplied equations and equations of standard major head loss. Minor head loss components were not considered and assumed trivial. Testing of the bladder prototype flow rate, however, proved that the flow resistance experienced by the device was greater than anticipated in the model. This unaccounted resistance is most likely due to unmodeled flow resistance through the valve manifolds that was initially considered negligible. The simplified piston-cylinder model, likewise, does not consider bulging during deflation of the bladders, which further introduces error. Future work of this model would most likely require empirical testing of all components of the valve system to generate more realistic models and, alternatively, an FEA simulation of the

bladders deflating. Further testing of the valves is outside the scope of this thesis and therefore, a bladder prototype that incorporated large holes for low-resistance air flow was utilized for the remainder of validation and testing procedures.

To validate contact models and analyze the prototype for slip-mitigation effects, a test was designed using the AFS to replicate an impact onto the prototype while in horizontal motion. The test utilized the AFS load cell to provide a constant horizontal velocity and a melamine board clamped to an aluminum plate that represent the ground slipping phenomena using wooden dowels. Large weights were suspended above the prototype and were released via a drive screw mechanism. The horizontal forces were recorded with the AFS load cell and the normal forces via the AFS Force Plate. The test produced some positive results, but unfortunately, video playback indicated flaws within the test set-up that could invalidate the load cell and force plate readings. These flaws included moment forces acting on the load cell due to the slight bending of the plate and wood as well as unaccounted damping effects throughout the plate and wood components. It was observed that a slight signal delay of roughly 40 ms was also apparent between the load cell and force plate readings. Investigations of this phenomenon are detailed below.

To explore these anomalies and validate contact models, a second test to verify the contact models without horizontal forces was performed that utilized the same set-up without the horizontal movement of the plate/board. The simplified model created an impulse that was analyzed and, when compared to the chosen Flores and Gonthier contact models, normal force was similar in amplitude. Factors of the normal force response such as settling time and damping coefficient are expected to be very different for humans due to the many complexities of the muscles, joints, and cognitive factors that affect response to movement. Since the amplitude of the response of the system was similar to the simulations, the contact models

were considered validated and attention was turned to testing horizontal force reactions during impulse.

To understand how horizontal forces changed during impact, the AFS was used to replicate the normal force impulse found in previous testing. However, it was noted in previous testing that normal force signals and horizontal force signals from the force plate and load cell, respectively, appeared out of phase by roughly 40 ms. To better understand this discrepancy, a simple test was devised that replicated the moving plate/board on a smaller and less complex scale while mitigating several sources of error such as bending moment forces and unaccounted damping factors. The test proved that an additional 6 ms delay between the load cell and force plate were present and subsequent investigation of the AFS control code revealed filtering mechanisms that most likely were accountable for this phenomenon. Therefore, data recorded from the AFS were altered to reflect this discrepancy for the remainder of the testing in this thesis and the remainder signal delay time was assumed to be a by-product of the testing apparatus.

The effects of impulse on horizontal or friction forces as well as the COF had yet to be determined as they were assumed to be best understood via empirical methods. Therefore, a test using the AFS to replicate the contact forces found within the aforementioned modeling and testing was designed. This test did not include the complex set-up previously used but, instead utilized a small plate rigidly attached to the load cell, moving on a Teflon-coated plastic sheet while exerting a force on the force plate. The test validated the assumption that COF between the two surfaces increases during large impacts.

This finding is exciting as, given enough impact force, the required COF of a surface could be momentarily increased during a slipping event that, with ample surface testing, could be used to transfer the slipping shoe from the less stable kinetic COF region to a more stable

static COF and thereby mitigate or reduce slip. It was mathematically shown that even with a constant COF, the impact generated during the collision could be used to significantly reduce the velocity or momentum of the person during slip. This result is useful in that given an orthotic device that can detect accelerations, the device could be actuated amid a slip event to prevent the user from reaching the dangerous slipping speeds of 0.5 m/s or critical distance of 10 cm. This is achieved either by reducing the speed to near zero so as to transfer the user from the kinetic COF to the static COF region as discussed above, or by granting the user more time to regain control of the slipping foot and recover from the slip before critical speeds or distances are reached.

However, testing in a similar manner using the bladder system and a shoe sole without mechatronic valves proved that there are several behaviors of the bladder system that are not yet understood. These tests subjected the prototype/sole combination to similar rapid increases in vertical force and displayed results different than those mentioned above. These odd behaviors will provide a direction for future work.

Future work should involve better modeling procedures of both air flow and bladder structure dynamics to better predict bladder behavior. Further validation efforts of the impulse equations being used as a slip-mitigating procedure will most likely need to be performed via human subject testing. This is necessary as the models and testing outlined in this thesis do not account for the complex movements of the human body, such as muscles, tendons, and joints, that could have effects on the device performance. These characteristics are difficult to model mathematically and are often best tested empirically via subject testing. Another factor that could influence device performance are proprioceptive cues and reactions from the user, which are also difficult to mathematically predict. Therefore, subject testing would add a great deal of knowledge to the device performance by incorporating “human” factors into the scenario.

However, before human subject testing can possibly occur, two further modifications with the orthotic device would need to be incorporated. The first modification includes developing a valve actuation system that can deflate the air bladders fast enough to generate significant impact with the ground surface. The simulation outlined in this thesis can be used to predict an approximate size of valve needed for adequate air flow. Other options for air flow include altering the existing flow restrictions with the current device, adding more valves, or using higher performance valves. However, these revisions are beyond the scope of this research and are left to future development. A second, more radical approach would be to utilize a completely mechanical system that incorporates two rigid plates acting as the top and bottom surfaces of sole and are held apart via a linkage system that can be actuated to allow the plates to create relative movement. Such a design would eliminate air flow restrictions but may also add significant weight to the orthotic device.

The final modification to the orthotic device is the ability to detect slip either before or during the slipping instance. Several more sensors and analyses will need to be performed and tested to create an algorithm that can reliably predict/detect slip and actuate the bladder system at an appropriate time. Both modifications are outside the scope of this thesis as this work serves as a preliminary testing process to prove that such a device could be used to mitigate slip. The results show that, given correct circumstances and device features, the proposed orthotic shoe sole device could be used to stop or mitigate human slip, thereby reducing injury and costs to the users.

REFERENCES

[1] L. M. S. R. Institute, "Top 10 Causes of Disabling Injuries 2007," Liberty Mutual Insurance Company, 175 Berkeley St., Boston, MA 02116, 2010.

[2] Y. Wang and M. A. Minor, "Design of a bladder based elastomeric Smart Shoe for haptic terrain display," in *Intelligent Robots and Systems*, Chicago, 2014.

[3] Y. Wang, C. Gregory and M. A. Minor, "Improving Mechanical Properties of Molded Silicone Rubber for Soft Robotics via Fabric Compositing," *Soft Robotics,* (Submitted March 2017).

[4] L. Srandberg and H. Lanshammar, "The Dynamics of Slipping Accidents," *Journal of Occupational Accidents,* vol. 3, no. 3, pp. 153-162, 1981.

[5] R. Cham and M. S. Redfern, "Heel Contact Dynamics During Slip Events on Level and Inclined Surfaces," *Safety Science,* vol. 40, no. 7, pp. 559-576, 2002.

[6] P. J. Perkins, "Measurment of Slip Between the Shoe and Ground During Walking," *Walkway Surfaces: Measurement of Slip Resistance,* pp. 71-87, 1978.

[7] Y. Wahab, M. Mazalan, N. A. Bakar, A. F. Anuar, M. Z. Zainol and F. Hamzah, "Low Power Shoe Integrated Intelligent Wireless Gait Measurement System," *Journal of Physics: Conference Series,* vol. 495, 2014.

[8] L. V. Nguyen, H. M. La, J. Sanchez and T. Vu, "A Smart Shoe for Building a Real-Time 3D Map," *Automation in Construction,* vol. 71, pp. 2-12, 2016.

[9] Y. Tao, "An Intelligent Shoe System for Health Detection and Enhancement," The Chinese University of Hong Kong, Hong Kong, 2014.

[10] H. Onodera, T. Yamaguchi, H. Yamanouchi, K. Nagamori, M. Yano, Y. Hirata and K. Hokkirigawa, "Analysis of the Slip-Related Falls and Fall Prevention with an Intelligent Shoe System," in *International Conference on Biomedical Robotics and Biomechatronics*, Tokyo, 2010.

[11] P. Fino and T. E. Lockhart, "Required Coefficient of Friction During Turning at Self-Selected Slow, Normal, and Fast Walking Speeds.," *Journal of Biomechanics,* vol. 47, pp. 1395-1400, 2014.

[12] K. E. Beschorner, D. L. Albert and M. S. Redfern, "Required Coefficient of Friction During Level Walking Is Predictive of Slipping," *Gait & Posture,* vol. 48, pp. 256-260, 2016.

[13] J.-s. Seo and S. Kim, "Asymmetrical Slip Propensity: Required Coefficient of Friction," *Journal of Neuroengineering and Rehabilitation,* vol. 10, no. 1, p. 1, 2013.

[14] R. Kikuuwe, N. Takesue, A. Sano, H. Mochiyama and H. Fujimoto, "Fixed-Step Friction Simulation: From Classical Coulomb Model to Modern Continuous Models," in *2005 IEEE/RSJ International Conference on Intelligent Robots and Systems*, 2005.

[15] M. Wojtyra, "Multibody Simulation Model of Human Walking," *Mechanics Based Design of Structures and Machines,* vol. 31, no. 3, pp. 357-379, 2003.

[16] A. Imura and M. Yeadon, "Mechanics of the Fouetté Turn," *Human Movement Science,* vol. 29, pp. 947-955, 2010.

[17] M. Jackson, M. Hiley and M. Yeadon, "A Comparison of Coulomb and Pseudo-Coulomb Friction Implementations: Application to the Table Contact Phase of Gymnastics Vaulting," *Journal of Biomechanics,* vol. 44, pp. 2706-2711, 2011.

[18] S. Lunzman, D. Kennedy and S. Miller, "Physical Modeling of Mechanical Friction in Simulink," *MATLAB Digest,* 2008.

[19] P. M. Wensing and D. E. Orin, "Generation of Dynamic Humanoid Behaviors Through Task-Space," in *IEEE International Conference on Robotics and Automation*, Karlsruhe, Germany, 2013.

[20] M. de Lasa, I. Mordatch and A. Hertzmann, "Feature-Based Locomotion Controllers," *ACM Transactions on Graphics,* vol. 29, no. 131, 2010.

[21] H.-W. Park, P. M. Wensing and S. Kim, "Online Planning for Autonomous Running Jumps," in *Robotics: Science and Systems*, 2015.

[22] H. Hertz, "On the Contact of Solids - on the Contact of Rigid Elastic Solids and on Hardness," in *Miscellaneous Papers*, London, Macmillan and Co., 1896, pp. 146-183.

[23] P. Flores, M. Machado, M. T. Silva and J. M. Martins, "On the Continuous Contact Force Models for Soft Materials in Multibody Dynamics," *Multibody System Dynamics,* vol. 25, no. 3, pp. 357-375, 2011.

[24] M. Machado, P. Moreira, P. Flores and H. M. Lankarani, "Compliant Contact Force Models in Multibody Dynamics: Evolution of the Hertz Contact Theory," *Mechanism and Machine Theory,* vol. 53, pp. 99-121, 2012.

[25] W. Goldsmith, Impact: The Theory and Physical Behaviour of Colliding Solids, London: Edward Arnold, 1960.

[26] D. P. Aguirre, "Multibody Modelization of a Biped Robot," in *Electrotechnical Conference (MELECON), 2012 16th IEEE Mediterranean*, 2012.

[27] Y. Gonthier, J. McPhee, C. Lange and J.-C. Piedbœuf, "A Regularized Contact Model with Asymmetric Damping and Dwell-Time Dependent Friction," *Multibody System Dynamics,* vol. 11, no. 3, pp. 209-233, 2004.

[28] S. Park and M. Minor, "Modeling and Dynamic Control of Compliant Framed Wheeled Modular Mobile Robots," *Robotics and Automation, 2004. Proceedings. ICRA '04. 2004 IEEE International Conference on,* vol. 4, pp. 3937-3943, 2004.

[29] K. Kondoh and S. Atluri, "Influence of Local Buckling on Global Instability: Simplified, Large Deformation, Post-Buckling Analyses of Plane Trusses," *Computers and Structures,* vol. 21, no. 4, pp. 613-627, 1985.

[30] "Mold Max Series," Smooth-On, [Online]. Available: http://www.smooth-on.com/Silicone-Rubber-an/c2_1113_1135/index.html. [Accessed Sept. 2014].

[31] P. Dahl, "A Solid Friction Model," Space and Missle System Organization, Air Force Systems Command, Los Angeles Air Force Station, 1968.

[32] C. C. de Wit, H. Olsson, K. Åström and P. Lischinsky, "A New Model for Control of Systems with Friction," *IEEE Transactions on Automatic Control,* vol. 40, no. 3, 1995.

[33] B. Jacobsen, "The Stribeck Memorial Lecture," *Tribology International,* vol. 36, no. 11, pp. 781-789, 2003.

[34] V. Lampaert, J. Swevers and F. Al-Bender, "Modification of Leuven Integrated Friction Model Structure," *IEEE Transactions on Automatic Control,* vol. 47, no. 4, 2002.

[35] J. Swevers, F. Al-Bender, C. G. Ganseman and T. Prajogo, "An Integrated Friction Model Structure with Improved Presliding Behavior for Accurate Friction Compensation," *IEEE Transactions on Automatic Control,* vol. 45, no. 4, 2000.

[36] J. J. Miller, M. A. Minor and A. S. Merryweather, "Design, Fabrication, Programming, and Evaluation of an Ankle Foot Simulator," Dept. of Mechanical Engineering, University of Utah, Salt Lake City, UT, 2016.

[37] T. L. Company, "Electro-Fluidic Systems Handbook," [Online]. Available: http://www.theleeco.com/resources/pdf/The%20Lee%20Company%20Electro-Fludic%20Systems%20Handbook%208th%20Edition.pdf. [Accessed June 2015].

[38] F. M. White, "Flow in a Circular Pipe," in *Fluid Mechanics 3rd Edition*, McGraw-Hill, Inc., 1994, p. 309.

[39] C. F. Colebrook, "Turbulent Flow in Pipes, with Particular Reference to the Transition between the Smooth and Rough Pip Laws," *J. Inst. Civ. Eng. Lond.,* vol. 11, pp. 133-156, 1938-1939.

[40] S. E. Haaland, "Simple and Explicit Formulas for the Friction Factor in Turbulent Pipe Flow," *Journal of Fluids Engineering,* vol. 105, no. 1, pp. 89-90, 1983.

[41] "Dry Air Properties," The Engineering Toolbox, [Online]. Available: http://www.engineeringtoolbox.com/dry-air-properties-d_973.html. [Accessed 31 5 2017].

[42] K. H. Hunt and F. R. E. Crossley, "Coefficient of Restitution Interpreted as Damping in Vibroimpact," *Journal of Applied Mechanics,* vol. 42, no. 2, pp. 440-445, 1975.

[43] "Shoe Size Averages," Statistic Brain Research Institute, [Online]. Available: http://www.statisticbrain.com/shoe-size-averages/. [Accessed 20 April 2017].